The Astrophysical Journal, 938:99 (18pp), 2022 October 20 https://doi.org/10.3847/1538-4357/ac88c8

Laboratory Study of the Cameron Bands and UV Doublet in the Middle Ultraviolet 180–300 nm by Electron Impact upon CO_2 with Application to Mars

Rena A. Lee[1,2], Joseph M. Ajello[1], Charles P. Malone[3], J. Scott Evans[4], Victoir Veibell[4], Gregory M. Holsclaw[1], William E. McClintock[1], Alan C. Hoskins[1], Sonal K. Jain[1], Jean-Claude Gérard[5], Saurav Aryal[1], and Nicholas M. Schneider[1]

[1] Laboratory for Atmospheric and Space Physics, University of Colorado, Boulder, CO, USA
[2] Department of Earth Sciences, University of Hawai'i at Mānoa, Honolulu, HI, USA
[3] Jet Propulsion Laboratory, California Institute of Technology, Pasadena, CA, USA
[4] Computational Physics Inc., Springfield, VA, USA
[5] University of Liège, Liège, Belgium

Received 2022 January 30; revised 2022 July 25; accepted 2022 August 9; published 2022 October 17

Abstract

We have observed electron impact fluorescence from CO_2 to excite the Cameron bands (CBs), CO ($a^3\Pi \rightarrow X\,^1\Sigma^+$; 180–280 nm), the first-negative group (1NG) bands, CO^+ ($B\,^2\Sigma^+ \rightarrow X\,^2\Sigma^+$; 180–320 nm), the fourth-positive group (4PG) bands, CO ($A\,^1\Pi \rightarrow X\,^1\Sigma^+$; 111–280 nm), and the UV doublet, CO_2^+ ($\tilde{B}\ ^2\Sigma_u^+ \rightarrow \tilde{X}\ ^2\Pi_g$; 288.3 and 289.6 nm) in the ultraviolet (UV). This wavelength range matches the spectral region of past and present spacecraft equipped to observe UV dayglow and aurora emissions from the thermospheres (100–300 km) of Mars and Venus. Our large vacuum system apparatus is able to measure the emission cross sections of the strongest optically forbidden UV transitions found in planetary spectra. Based on our cross-sectional measurements, previous CB emission cross-sectional errors exceed a factor of 3. The UV doublet lifetime is perturbed through $\tilde{B}\ ^2\Sigma_u^+ - \tilde{A}\ ^2\Pi_u$ spin–orbit coupling. Forward modeling codes of the Mars dayglow have not been accurate in the mid-UV due to systematic errors in these two emission cross sections. We furnish absolute emission cross sections for several band systems over electron energies 20–100 eV for CO_2. We present a CB lifetime, which together with emission cross sections, furnish a set of fundamental physical constants for electron transport codes such as AURIC (Atmospheric Ultraviolet Radiance Integrated Code). AURIC and Trans-Mars are used in the analysis of UV spectra from the Martian dayglow and aurora.

Unified Astronomy Thesaurus concepts: Carbon dioxide (196); Mars (1007); Molecular physics (2058); Radiative processes (2055); Molecular spectroscopy (2095); Experimental techniques (2078); Collisional processes (2286)

1. Introduction

There have been five spacecraft missions to Mars in the last 50 yr equipped with state-of-the-art UV spectrographs to observe the Mars dayglow and aurora in the midultraviolet (MUV; 180–340 nm): Mariner 6, 7, and 9 (Barth et al. 1971, 1972, 1973), Mars Express (MEx; Bertaux et al. 2006), and the Mars Atmosphere and Volatile Evolution (MAVEN) Mission (Jakosky et al. 2015). The atmosphere of Mars is dominated by CO_2, CO, O, and N_2 gases (Hubert et al. 2010; Evans et al. 2015; Jain et al. 2015; Stevens et al. 2015). The MAVEN and MEx spacecraft make orbital measurements, as does the recent Emirates Mars Mission (Al Matroushi et al. 2019; Holsclaw et al. 2021), observing UV atmospheric glow intensities from these dominant species to study Mars' thermosphere–ionosphere coupling with the space environment (Simon et al. 2009; González-Galindo et al. 2018; Gérard et al. 2019). The observations are made in three UV wavelength ranges: in the extreme-ultraviolet (EUV; 80–120 nm), far-ultraviolet (FUV; 110–190 nm), and MUV (180–340 nm). The physics and chemistry of the upper atmospheric evolution of Mars and Venus can be determined from the analysis of UV atmospheric glow spectra by MAVEN IUVS (Imaging Ultraviolet Spectrograph, 110–340 nm), MEx SPICAM, and VEx SPICAV (SPectroscopy for Investigation of Characteristics of the Atmosphere of Mars and Venus, respectively, 118–320 nm), and the Emirates Ultraviolet Spectrometer, 85–185 nm). The separation of the various excitation processes in forward modeling requires emission cross sections for photoelectron and auroral electron excitation, dissociative recombination, and solar fluorescence of major molecular constituents: CO_2, CO, O, and N_2 (Evans et al. 2015).

Mars and Venus have atmospheres that are similar in composition and have nearly identical UV dayglow spectra (Hubert et al. 2010; Chaufray et al. 2012; Gérard et al. 2017). As motivation for our spectral and cross-sectional study of CO_2, we show in Figure 1(a) the IUVS MUV limb dayglow spectrum of Mars at 150 km altitude (Jain et al. 2015) overplotted with two optically thin MUV fluorescence spectra of electron excitation of CO_2 at two low (20 and 30 eV) electron energies measured in the laboratory with the MAVEN IUVS BreadBoard (BB), serving as the flight spare, prior to launch. These electron energies are typical of the Mars mean photoelectron distribution measured by the Solar Wind Electron Analyzer (SWEA) on board MAVEN. We also display an IUVS MUV aurora spectrum (Soret et al. 2021) in Figure 1(b) overplotted with the same 30 eV laboratory spectrum. SWEA (Mitchell et al. 2016) is a part of the Particles and Fields package and measures the solar wind and ionospheric electrons, as shown in Figure 2. The mean photoelectron energy at 125–135 km altitude is found to be 21.5 eV. Both calibrated MUV laboratory spectra are

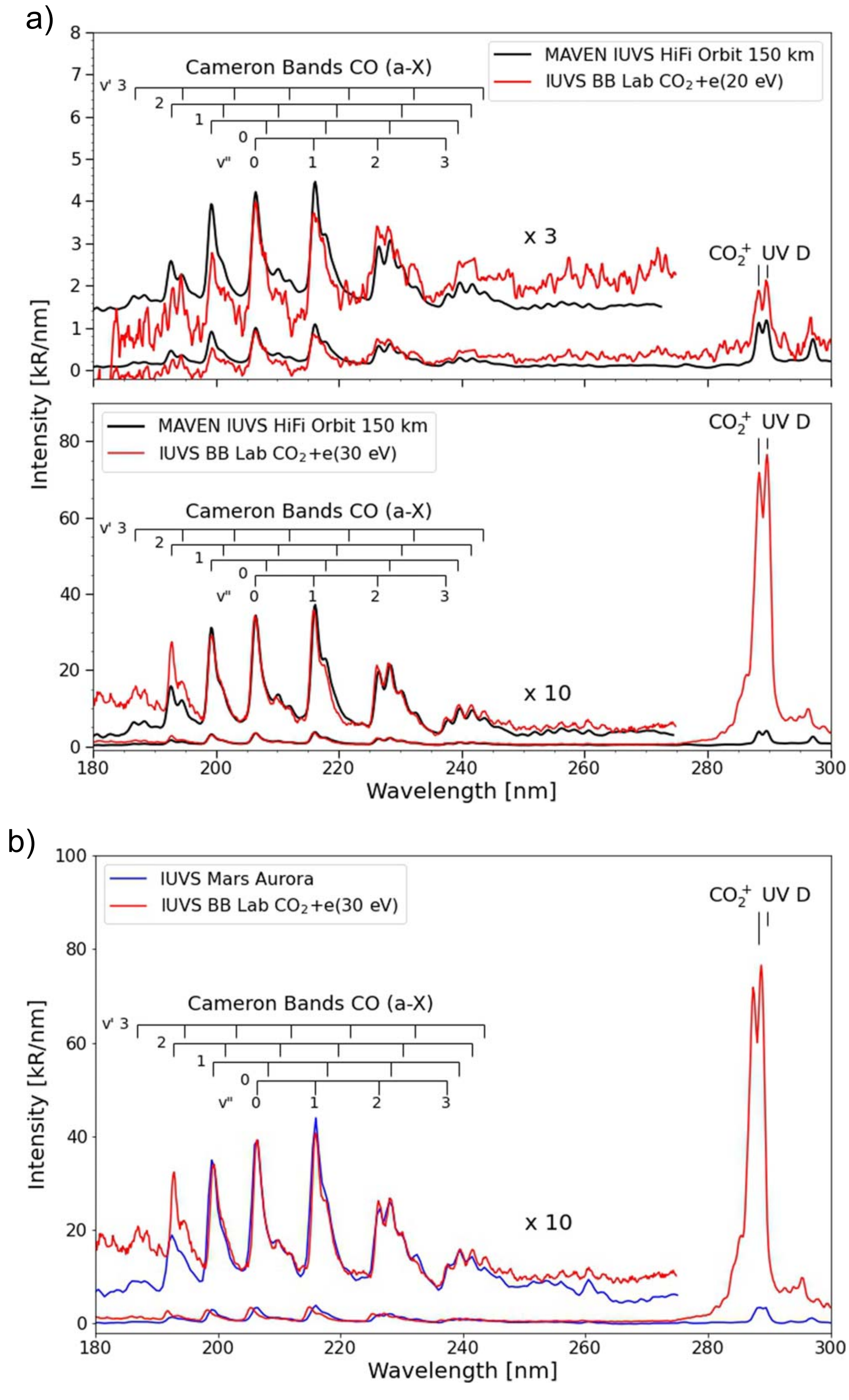

Figure 1. (a) Comparison of MUV spectra produced in the laboratory by the single-scattering electron excitation of CO_2 gas at 300 K at 20 eV (top) and 30 eV (bottom) impact energy with Mars IUVS MUV dayglow spectrum from a periapsis pass at 150 km minimum ray height (Jain et al. 2015). The mean spectrum at 150 km is taken from average data from MAVEN orbits 2957–3221 (∼170 orbits; Ls: 133–158; dates: 2016 June 4 to 2016 May 5). (b) A comparison of MUV spectra produced in the laboratory by the single-scattering electron excitation of CO_2 gas at 300 K at 30 eV impact energy with Mars IUVS MUV averaged auroral spectrum (Soret et al. 2021).

normalized to the Cameron band (CB) (0, 1) at 216 nm measured in the dayglow by MAVEN IUVS at 150 km altitude in the thermosphere in 2015 (Jain et al. 2015). The laboratory-generated monoenergetic electron impact fluorescence and Mars airglow MUV spectra indicate the same MUV emissions from the two strongest band systems: the CO CBs and CO_2^+

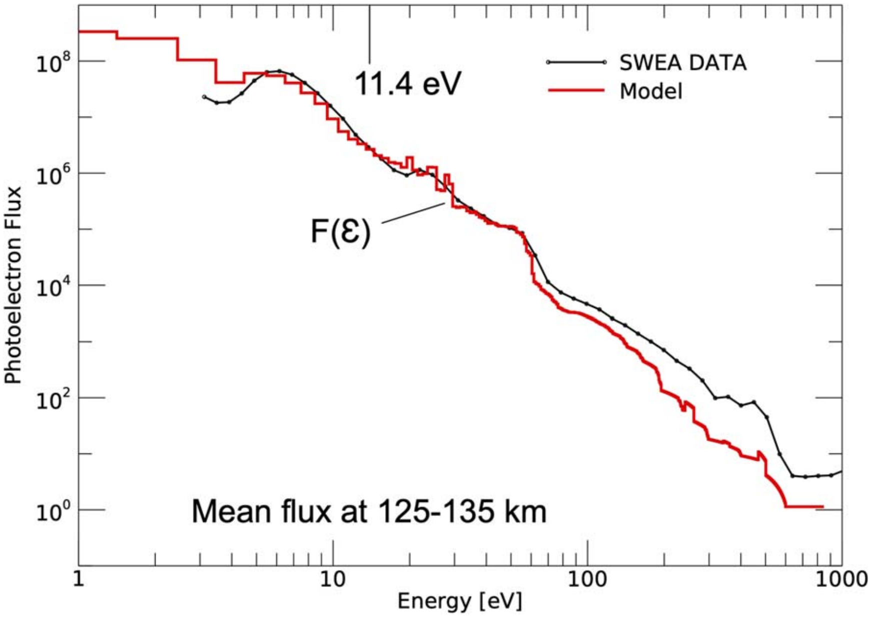

Figure 2. Measurement by SWEA of the mean photoelectron flux in the Mars ionosphere (125–135 km) (Mitchell et al. 2016; Xu et al. 2017) during MAVEN orbit 6958 (2018 April 28) with a model (Jain & Bhardwaj 2012) showing the mean electron energy is 21 eV, an energy above the CB threshold of 11.4 eV. F(ε) is the photoelectron energy distribution function (see Equation (1)) in the altitude range of 125–135 km.

UV doublet (UVD). We observe that the two sets of CBs have similar vibrational band intensities as indicated in Figures 1(a) and (b). Both MUV measurements, one on Earth in the laboratory and the other on Mars positioned to observe the Mars limb at a minimum ray height of 150 km, are observed with an identical instrument pair: the IUVS flight instrument and the IUVS BB.

Dayglow and aurora modeling studies of the main emissions, CB, CO ($a\,^3\Pi \rightarrow X\,^1\Sigma^+$; 180–280 nm), fourth-positive group (4PG), CO ($A\,^2\Pi \rightarrow X\,^1\Sigma^+$, 130.0–190.0 nm), the first-negative group (1NG), CO$^+$ ($B\,^2\Sigma^+ \rightarrow X\,^2\Sigma^+$; 180–320 nm), CO$_2^+$ ($\tilde{A}\ ^2\Pi_u \rightarrow \tilde{X}\ ^2\Pi_g$ 280–500 nm), Fox–Duffendack–Barker (FDB), and CO$_2^+$ UVD ($\tilde{B}\ ^2\Sigma_u^+ \rightarrow \tilde{X}\ ^2\Pi_g$; at 288.3 and 289.6 nm) band systems, require MUV emission cross sections of CO$_2$ to complement our recent emission cross-sectional studies of CO by electron impact (Lee et al. 2021). Electron excitation of CO and CO$_2$ can produce the same MUV band systems, but with unique vibrational distributions and different rotational thermal energies. The vibrational distribution can be used as a basis to infer the mixing ratio variation with an altitude of these two main neutral atmospheric gases in the Martian and Venusian thermospheres. Modeling studies cannot presently be conducted with the same accuracy as the planetary measurements, which have state-of-the-art calibrated spectrographs (Bertaux et al. 2006; Simon et al. 2009; Jain et al. 2015; Jakosky et al. 2015; McClintock et al. 2015; González-Galindo et al. 2018; Gérard et al. 2019; Soret et al. 2021). This has created a dichotomy in accuracy between planetary observations and models because the atomic and molecular emission cross sections of these salient emissions have never been accurately measured in the laboratory as pointed out by Gronoff et al. (2012) and Simon et al. (2009).

Several recent planetary dayglow analysis papers show marked discrepancies between measurement and models due to the flawed CB cross sections employed. For example, Chaufray et al. (2012) could not explain the observed Venusian ratio of CB to UVD of 7.4 at the peak of the dayglow. They also point out that the models of CB on Mars are overestimated due to an overestimate of CO ($a\,^3\Pi$) UV emission cross section from electron impact. The same ratio on Mars from SPICAM is about 5. Gérard et al. (2019) analyzed MUV dayglow spectra acquired by MAVEN IUVS at different seasons and obtained ratios ranging from 4.7–5.7. González-Galindo et al. (2018) found that to properly explain the modeling of CB production for the Mars dayglow by electron impact dissociative excitation of CO$_2$, the UV emission cross section must be reduced by a factor of 3 from the values of Erdman & Zipf (1983) or Avakyan et al. (1998). Several models in the literature (Shematovich et al. 2008; Cox et al. 2010; Gronoff et al. 2012; Jain & Bhardwaj 2012; González-Galindo et al. 2018) already applied an empirical correction to the Avakyan et al. cross section. They divided its value by a constant factor of 2 or 3 at all energies. Exceptions were Fox & Dalgarno (1979) who used a peak value of 4×10^{-17} cm^2 at 27 eV while the model of Simon et al. (2009) and the Monte Carlo calculations by Gérard et al. (2019) were based on the original Avakyan et al. values with a peak value of 2.4×10^{-16} cm^2.

The uncertainties of particular emission cross sections of UV transitions are greater than 100%. Our current set of UV laboratory spectra (35% accuracy) from low energy electron impact of CO, CO$_2$, and N$_2$ provide a key opportunity for allowing more rigorous forward modeling of dayglow and aurora (Gronoff et al. 2012; Ajello et al. 2017, 2019, 2020; Lee et al. 2021).

2. Historical Background

The measurements of laboratory UV emission cross sections from electron impact fluorescence published prior to 1998 from allowed and optically forbidden transitions are archived in a handbook (Avakyan et al. 1998) from published emission cross sections of the previous 50 yr. Emission cross sections determine the emission rate of each UV transition in the atmosphere. For a planetary atmosphere the dayglow emission rate, $g_{m,k}$ (photons cm^{-3} s^{-1}) of species m, from rovibrational electronic state k, involving electron impact of energy, ε, at altitude z is determined by the following expression, which involves a product of three terms, inside an integral over electron energy and a summation over the rovibrational levels of the ground electronic state, α,

$$g_{m,k}(z) = \Sigma\left[N_m(z,\, T)\int F(\varepsilon,\, z)\sigma_{m,k}(\varepsilon)\; d\varepsilon\right], \tag{1}$$

where $F(\varepsilon,z)$, is electron flux at altitude z, $N_m(z,T)$ is the molecular density of the thermosphere constituent of species m in the ground rovibrational electronic state (α, v'', j'') at altitude z and temperature T, and $\sigma_{m,k}(\varepsilon)$, is the emission cross section of the rovibrational electronic state, (k, v, j), while $\sigma_{m,k}^{\rm em} = \sigma_{m,k}^{\rm emdirect} + \sigma_{m,k}^{\rm emcascade} - \sigma_{m,k}^{\rm predissociation}$. Two of these variables in Equation (1) are provided by spacecraft instrumentation, namely the electron flux at altitude z as a function of energy ε, and number density $N_m(z,T)$ in the ground state. The emission cross section of rovibrational electronic state $\sigma_{m,k}(\varepsilon)(k,\ v,\ j)$ must be measured in the laboratory.

Our unique experimental imaging instrument with a wide field-of-view (FOV) can measure particle (e.g., electron, ion) excitation mechanisms and the resulting UV emission cross sections in like manner as the processes are occurring in a planetary atmosphere with long optical path lengths for long-lived states. The large vacuum chamber with imaging capabilities in the vacuum-ultraviolet (VUV) is ideal (and necessary) for the measurements of optically forbidden transitions presented in this paper. This apparatus spatially allows the experiment to distinguish optically forbidden transitions such as the CBs, and more generally the emissions originating from competing excitation processes, both allowed and forbidden. In previous studies, we have measured two competing optically forbidden processes to isolate spectral measurements in the laboratory of single-scattering electron-impact-induced fluorescence from two Lyman–Birge–Hopfield (LBH) emission processes: direct excitation, which is strongest in emission near the electron beam axis; and cascade induced, which is dominant far from the electron beam axis (Ajello et al. 2017, 2020). In particular, the MUV emission cross sections of the optically forbidden CB and the forbidden perturbations of the UVD band system by the $\tilde{A}\ {}^2\Pi_u$ spin–orbit coupling are the primary goal of this work.

Most of the strong optically forbidden UV emissions from dominant planetary gases (H_2, N_2, O_2, CO, and CO_2) have been fully identified by planetary spectra of the upper atmosphere. However, their concomitant physical properties (single-scattering laboratory rotationally resolved spectra and emission cross sections) have never been fully measured in the laboratory by conventional low-resolution UV spectroscopy operating with inadequately sized ($\sim$10 cm radius) collision chambers.

Accurate planetary and terrestrial atmosphere modeling of the optically forbidden LBH transitions was not possible until recently due to inaccurate laboratory-measured emission cross sections, which failed to present the complete glow pattern of LBH emission. The study of the LBH band system ($a^1\Pi_g \rightarrow X\ {}^1\Sigma_g^+$) of N_2 in the laboratory by UV spectroscopy had, until now, failed to measure the cascade-induced UV spectrum and determine LBH vibrational intensities or cascade emission cross sections. This failure precipitated a controversy in the literature that has persisted for decades, due to the dichotomy between terrestrial airglow observations and model calculations (Cartwright 1978; Budzien et al. 1994; Eastes & Dentamaro 1996; Eastes 2000). We have, for the first time, measured the UV forbidden LBH emissions at the University of Colorado with a large (1.5 m diameter chamber) vacuum system apparatus, using a long focal length electrostatic electron gun at low electron energy (10–200 eV), providing a long optical path length without excited-molecule deactivation from wall collisions (Ajello et al. 2017, 2019, 2020; Lee et al. 2021).

The study of CB atmospheric excitation rates is the focus of the present laboratory aspect of this paper; the four contributing electron and photon CB processes (a)–(d) contain the following cross sections ($\sigma_{\rm em}$):[6,7,8,9]

$$CO_2\ (\tilde{X}\ {}^1\Sigma_g^+) + e\ \rightarrow\ CO\ (a\ {}^3\Pi) + O + e', \tag{a}$$

$$CO\ (\tilde{X}\ {}^1\Sigma^+) + e\ \rightarrow\ CO\ (a\ {}^3\Pi) + e', \tag{b}$$

$$CO_2\ (\tilde{X}\ {}^1\Sigma_g^+) + h\nu\ \rightarrow\ CO\ (a\ {}^3\Pi) + O, \tag{c}$$

$$CO_2^+\ (\tilde{X}\ {}^2\Pi_g) + e\ \rightarrow\ CO\ (a\ {}^3\Pi) + O. \tag{d}$$

Simon et al. (2009) point out that the photon (process (c)) and dissociative recombination (process (d)) mechanisms are better known. We have greatly improved upon the uncertainty from 200% to less than 35% in the CO ($a\,{}^3\Pi$) MUV CB emission cross section from e^-+CO (process b) (Lee et al. 2021). We recently measured in the FUV the 4PG CO ($A\ {}^1\Pi$) emission cross section (Ajello et al. 2019). Process (a) is the remaining emission cross section needed to fully understand the MUV limb spectra of IUVS, SPICAM, and SPICAV to separate the CO and CO_2 contributions to the CB. The largest uncertainties remain on the CB production of CO ($a - X$) emission by electron impact on CO_2, which has been reported but by a highly flawed measurement from 50 yr ago (Ajello 1971b). We address process (a) in this paper.

The flaws in the Ajello (1971b) measured cross section of the CB (the only previous absolute measurement of the CB emission cross section from e+CO_2) have been pointed out by Erdman & Zipf (1983). The CB cross section observed by Ajello (1971b) relied on an experimental chamber insufficiently large to fully observe the CB, as the high-velocity excited CO(a) state molecules were deactivated in collisions with the chamber walls. Furthermore, the CB system was not fully resolved due to spectral blending with the 4PG band system. Erdman & Zipf (1983) recommended an absolute value of 2.4×10^{-16} cm^2 at 80 eV. Avakyan's cross section reaches 2.0×10^{-16} cm^2 at 80 eV. Other authors such as Fox & Dalgarno (1979, 1981) and Fox (2008) chose different values, i.e., 4×10^{-17} cm^2 at 27 eV, derived from Freund (1971). We recommend abandoning the previous CB work of Ajello (1971a, 1971b) based on more accurate work in this experiment, which avoids the effects of uncertainty in spectral blending, measures the entire band system from 180–280 nm, and includes an accurate accounting for the kinetic energy-imparted drift out of the detector FOV from dissociative excitation of CO_2 to excite the $a\,{}^3\Pi$ molecules as measured in the CB glow (see Section 6).

The entire problem of UV emission cross-sectional discrepancies that have accumulated in the last 50 yr has begun to be explained by Ajello et al. (2017, 2019, 2020) and Lee et al. (2021). The excitation processes prevalent in the upper

---

[6] $\sigma_{\rm em}$ (Ajello 1971a; Erdman & Zipf 1983; Avakyan et al. 1998),

[7] $\sigma_{\rm em}$ reported Lee et al. (2021).

[8] CO yield reported by Lawrence (1970, 1972).

[9] CO yield reported by Skrzypkowski et al. (1998).

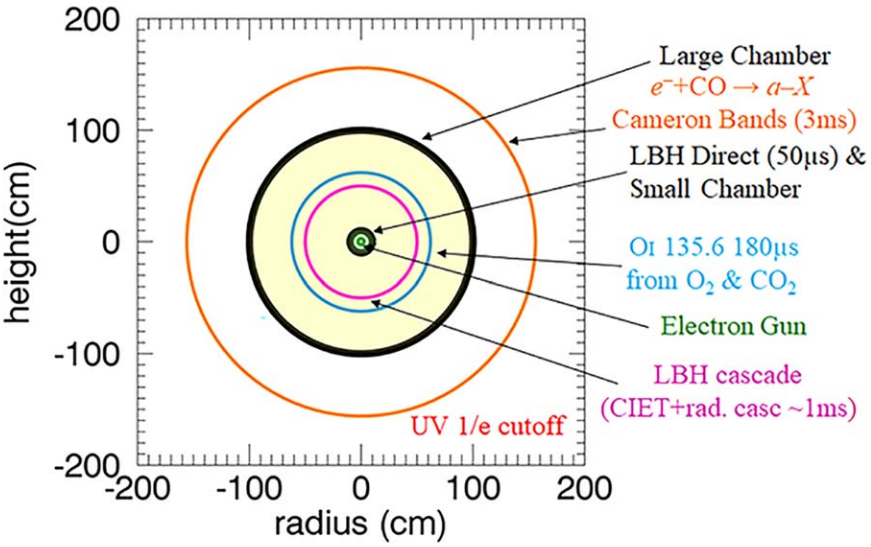

Figure 3. The 1/e radiative mean-free path for various optically forbidden transitions in two vacuum chambers is shown in black. The inner black 10 cm circle was the vacuum chamber size employed in laboratory experiments for the past 50 yr in laboratories around the world where chambers were built for allowed transitions with typical lifetimes of 10 ns or less, e.g., H Lyα. The outer black circle is a 1 m radius producing a glow pattern nearly identical to the 0.75 m radius of MOBI and allowing for the first studies of optically forbidden transitions like the LBH band system ($a\,^1\Pi_g \rightarrow X\,^1\Sigma_g^+$) of N_2 inside the outer black circle of MOBI or CO ($a\,^3\Pi$) $\rightarrow X\,^1\Sigma_g$. A thermal velocity excited CO ($a\,^3\Pi$) molecule will travel a mean distance of 1.56 m once excited on the axis of the electron gun, compared to a collisional mean-free path of ∼4 m for experimental conditions. The IUVS BB captures 62% of the radiation with Image 1 + Image 2 + Image 3 observing to a minimum ray height of 400 mm with 38% of excited CO(a) molecules deactivated at the walls of the experimental chamber.

atmospheres at the planets have not been duplicated in the laboratory until now, i.e., the event of single-scattering excitation and emission by optically forbidden UV transitions. We have found that many allowed (fast) transitions are also accompanied by either a slower cascade process or are perturbed in mixed levels as described by Lefebvre-Brion & Field (2012). In the low-resolution experiments (∼0.1–1 nm) such as those performed in most measurements in Avakyan et al. (1998), a small chamber will neglect to measure the slow cascade due to wall collisions. Our glow profiles indicate many electronic states are heavily perturbed by nearby electronic states in near energetic resonance. The glow profiles will show either a bi-exponential radial dependence or a glow profile indicative of an accompanying slow decay (Lefebvre-Brion & Field 2012; Ajello et al. 2017, 2019, 2020).

Figure 3 shows graphically that long radiative lifetime effects from optically forbidden transitions can lead to wall collisions where we have plotted the mean-free path of the optically forbidden atom or molecule at thermal velocity or 1 eV, the latter if a repulsive dissociation curve is involved. The opportunity to observe an optically forbidden transition can be fully or partially met by our 0.75 m chamber radius, similar to the 1 m chamber radius plotted in Figure 3 (Ajello et al. 2017, 2020) as compared to 10 cm radius chambers used in the past by most experimental apparatus (Ajello 1970). Note the two black circles in the figure that represent the 10 cm and 1 m radius chamber. We fully capture moderately fast radiative optically forbidden cascade with ∼1 ms lifetime.

The combined energy level diagram of CO_2 and CO_2^+ is shown in Figure 4 (adapted from Herzberg 1966). The CB MUV intensity that can be measured within the range of motion of the IUVS in the experimental chamber is 56%. The ∼1 eV escape energy of the CO($a\,^3\Pi$) excited molecule is schematically indicated in Figure 4. Our glow profile work is described in the next section and Section 6. Previous high-resolution laboratory spectra of fast O atoms formed in the dissociation of CO indicate an escape energy in the range of 0.5–5 eV kinetic energy (Beegle et al. 1999). The CO ($a\,^3\Pi$) excited molecule can be produced by predissociation of excited state CO_2^* by a repulsive potential energy curve (CO–O), most likely by following one of the two stretching C–O normal coordinates that at large separation are indicative of dissociation. This then becomes, as pointed out by Herzberg (1966), the pair: CO ($^1\Sigma$) + O (^{1}D) requiring 5.45 eV dissociation energy, or for CB production, CO ($a\,^3\Pi$) + O (^3P) requiring 11.46 eV dissociation and excitation energy. Direct dissociation of a repulsive state CO_2^* is also possible and indicated schematically in Figure 4.

3. Experimental Apparatus and Procedure

Our experimental apparatus has been described previously for FUV studies (Ajello et al. 2017, 2019, 2020) and for MUV studies (Lee et al. 2021). In brief, we have measured accurate FUV emission cross sections of two of the strongest optically forbidden transitions found in the terrestrial and Mars airglow: the LBH bands from electron impact fluorescence of N_2 (Ajello et al. 2017, 2020) and O I (135.6 nm) from electron impact fluorescence of CO and CO_2 (Ajello et al. 2019). In the MUV, we have recently reported the emission cross sections of the CB from electron impact excitation of CO (Lee et al. 2021). We published the initial work 19 yr ago for O I (135.6 nm) from the dissociation of O_2 using the Cassini Ultraviolet Imaging Spectrograph BreadBoard (UVIS BB; Kanik et al. 2003; Makarov et al. 2003). In the present study, we have used the MAVEN IUVS BB with a flight spare detector to observe and image the dipole-allowed and dipole-forbidden emissions occurring in the MUV to accurately study the CB spectrum from electron impact excitation of CO_2.

The experimental procedure is a replication of that of Ajello et al. (2019). An electron beam with an energy resolution of ∼1 eV was passed through static CO_2 gas with ionization gauge corrected chamber pressures of $2–2.5 \times 10^{-5}$ Torr

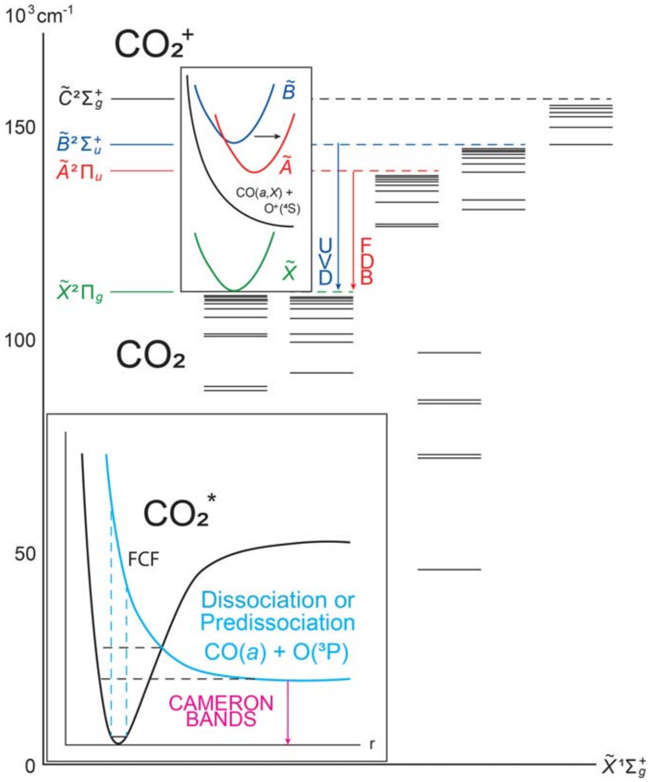

Figure 4. Energy level diagram of CO_2 and CO_2^+. Adapted from a combination of published schematic figures (Herzberg 1966, 1971; Leach et al. (1978; Tanaka et al. 1960). The top figure indicates the MUV ionic transitions; CO_2^+ UVD ($\tilde{B}\ ^2\Sigma_u^+ \rightarrow \tilde{B}\ ^2\Pi_g$; at 288.3 and 289.6 nm) and CO_2^+ FDB ($\tilde{A}\ ^2\Pi_u \rightarrow \tilde{X}\ ^2\Pi_g$; at 290–450 nm). The 100% dissociation and predissociation of the $\tilde{C}\ ^2\Sigma_g^+$ ionic state are shown to form the CBs CO ($a\ ^3\Pi$) + O (^3P) + e among other limits (Samson & Gardner 1973; Tsurubuchi & Iwai 1974). The bottom half of the figure indicates with dashed black lines a radiationless predissociation between two excited electronic states: CO_2^* (bound and repulsive; see Figure 185 of Herzberg 1950 as an example with predissociation selection rule criteria for diatomic molecules or Herzberg (1966) for polyatomic molecules) where the bound ground state of CO_2 is not shown but indicated schematically for the CB transition to CO(X) + O. Not shown but listed is a direct dissociation from an attractive CO_2 bound state into CO(a $^3\Pi$) + O (^3P) continuous state.

($n = 7$–9×10^{11} cm^{-3}) and a gas swarm temperature of 300 K. The cylindrical emission glow profile produced about the electron beam was measured up to a radial distance of ~400 mm. The IUVS BB was mounted to a vertically moving stage (see Figure 2 of Ajello et al. 2017 for an experimental schematic) and translated upward from the electron beam centered initially at 0 mm. Each spatial pixel spans an object region of 0.220 mm. The MUV spectral image was obtained in first spectral order by the IUVS BB yielding about 0.16 nm per channel with a measured spectral resolution of ~1.2 nm FWHM in the plane of dispersion (see Figure 5 for an example at 50 eV). Three overlapping images were taken at different stage positions to capture the glow region from long-lived states such as CO ($a\ ^3\Pi$). We can vary the vertical height of the placement of the optic axis of the IUVS BB at three positions above the electron beam axis. We begin the measurements from Image 1 on center (z = 0) with the emission from dipole-allowed transitions centered near spatial pixel 500, followed by a motion in the z-direction to obtain Image 2 centered at 15.24 cm (6 inches), and Image 3 centered at 30.48 cm (12 inches) above the electron beam.

4. MUV Electron Impact Spectra of CO_2

The MUV sensitivity calibration was discussed in Lee et al. (2021). The calibrated MUV spectra for each of the three images, as well as the summed total spectrum, are shown in Figure 6 for CO_2 from electron impact fluorescence at 30 eV from 180–300 nm. The same procedure was applied at the other energies studied: 20, 40, 50, and 100 eV. To our knowledge, these are the first calibrated MUV spectra of CO_2 with a large enough chamber to fully sample dipole-allowed and optically forbidden emissions and to account for a loss of CO ($a\ ^3\Pi$) excited molecules to the walls. The wavelength range for the strong observed CB system is 180–280 nm, with less than 5% contribution from 280–340 nm from either direct dissociative excitation into the a-state by various dissociation limits, or cascade from high-lying triplet states, as shown in Figure 4. The vibrational level tick marks of the CB are depicted in detail in the spectra in Figure 6.

LeClair & McConkey (1994) point out that both excited triplet and singlet states of CO_2 contribute to CO ($a\ ^3\Pi$ production through predissociation or direct dissociation, as also indicated in Figure 4. The CO_2^+ UVD ($\tilde{B}\ ^2\Sigma_u^+ \rightarrow \tilde{X}\ ^2\Pi_g$) can be identified at 288.3 and 289.6 nm. Both band systems have considerable long-lived contributions in the millisecond regime as judged by the strong cascade contribution for CO ($a\ ^3\Pi$) molecules and perturbation contributions for CO_2^+ ($\tilde{B}\ ^2\Sigma_u^+$) to the total spectra from Images 2 and 3. A further discussion of the glow profile follows in Section 6 (Ajello et al. 2017, 2019).

The previously published uncalibrated electron impact MUV spectra of CO_2 at 50 and 75 eV were obtained in a small vacuum chamber with a small FOV (Ajello 1971b). These spectra were only capable of showing the dipole-allowed direct-excitation contributions (analogous to our Image 1), without providing sufficient information on long-lived lifetime contributions to Image 1 from optically forbidden excitation. The previously measured Image 1 spectra from CO_2 and CO were pictorially shown (uncalibrated), respectively, in the work of Ajello (1971a, 1971b) and were analytically intercompared after calibration for cross-sectional analysis. However, a MUV 20 eV e+CO_2 electron impact uncalibrated spectrum by Erdman & Zipf (1983) clearly identified that the only observable molecular features arise from CB with substantial emission from 240–265 nm from the (v', $v' + \Delta v = 3$, 4) progressions.

To emulate a slight wavelength dependence in the data, a separate point-spread function (PSF) was derived for each of the two fits. The first fit modeled the wavelength range of 180–300 nm to include the strong CO_2^+ UVD source. The second fit was limited to 180–270 nm so that any slight imperfections in the dominant UVD source did not drastically interfere with other weaker sources. The PSF for the UVD-inclusive fit was determined via an optimization routine using the 30 eV O I 297.2 nm source, which was measured with the same BB instrument and vacuum chamber but with a CO gas (Lee et al. 2021). The PSF for the CB-focused fit was a Voigt function optimized using the 30 eV C I 193.1 nm source in the CO_2 data. We note the observation of molecular features on the blue side of the UVD band system. Current UVD band models do not adequately capture these observed molecular features, nor do any of the other band systems included in the fits to the CO_2 electron impact fluorescence measurements. These features have also been observed in MAVEN IUVS flight data

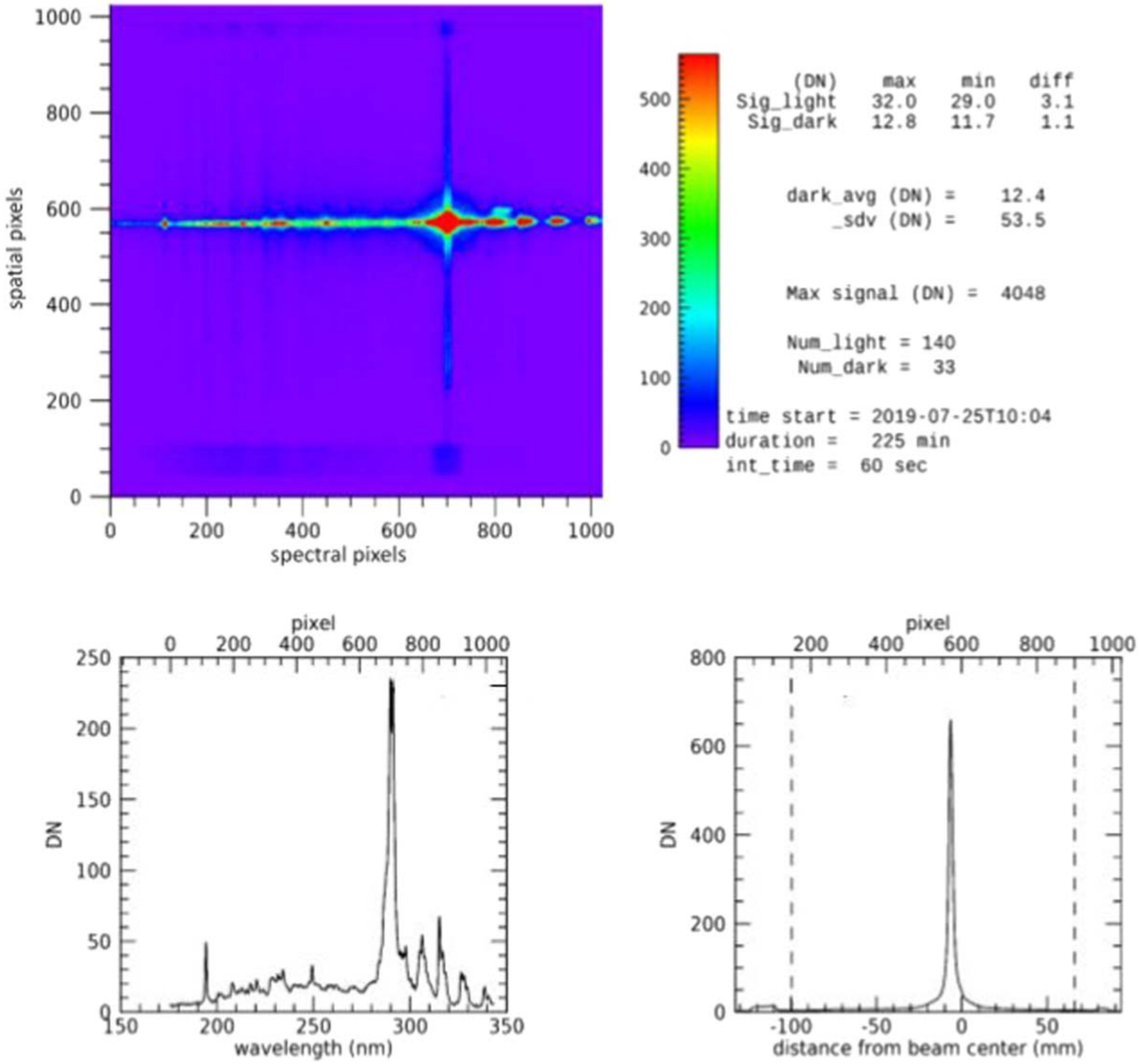

```
    (DN)      max    min   diff
Sig_light    32.0   29.0    3.1
 Sig_dark    12.8   11.7    1.1

   dark_avg (DN) =    12.4
       _sdv (DN) =    53.5

 Max signal (DN) =   4048

   Num_light = 140
    Num_dark =  33
time start = 2019-07-25T10:04
duration =   225 min
int_time =  60 sec
```

Figure 5. Details of the IUVS-OEU MUV imaging channels. Upper left: uncalibrated Image 1 file of e+CO_2 (50 eV) measurements showing 1024 × 1024 spatial and spectral pixels. The image is formed from electron impact direct excitation of CO_2. The spectrum is highlighted in the MUV by CBs, 1NG, and 4PG. We use spatial pixels 150:900, where the effects of internal scattering for the narrow slit are minimized. The broad occultation slit at the top of the IUVS extends from spatial pixels 50:150 in the image, and the smaller occultation slit at the bottom extends from spatial pixel 950:1000 and views the region above the electron beam as the IUVS moves vertically upward. Upper right: engineering readouts—detector temperature (°C) and minimum and maximum signal (counts per minute) variations observed during the measurement. Bottom left: mean e+CO_2 (50 eV) MUV uncalibrated spectrum in the narrow slit, averaged over spatial pixels 150:900 in units of counts over wavelength in nanometers. Bottom right: spatial intensity of MUV integrated first order intensity from e+CO_2 in units of counts with distance from the electron beam in millimeters.

(Jain et al. 2015). A possible source of these observed features is the (01^10)–(01^00) sub-band of the UVD band system (Gauyacq et al. 1975); however, further investigation and additional modeling are needed.

Ajello et al. (2019) used a Powell optimization routine based on maximizing Pearson correlation to fit the rotational temperature used to model CO 4PG bands. The rotational temperature determined for electron impact dissociation of CO_2 was 4800 K. We have adopted the same rotational temperature for the fits reported in the present study. Similarly, the optimal CB rotational temperature was found to be 3000 K based on a fit to a subset of bands from 190–220 nm, as shown in Figure 7. Similarly, we determined an optimal rotational temperature of 295 K for the CO^+ 1NG model templates, which was derived from fits to the measured spectra, and is consistent with the results reported by Conway (1981).

The calibrated spectra and multiple linear regression (MLR) results from this new study showing the atomic and molecular features follow. CO_2 electron impact fluorescence measurements at five electron energies of 20, 30, 40, 50, and 100 eV are considered. All energies were observed at a tank gas pressure of 2–2.5 $\times 10^{-5}$ Torr using the standard ionization gauge correction for CO_2. The spectra used for each energy were a summation of three observations on and above the electron beam axis in units of counts. These observations were summed across the spatial pixels [130–940] in the middle of the detector window, and limited in wavelength to 175–300 nm.

The MLR analysis of the laboratory spectra at each energy is shown in Figure 8 and consists of several independent model components: (1) an optically thin electron-impact-induced-fluorescence spectra (EIFS) model for each band system observed—the 4PG CO ($A\,^1\Pi \rightarrow X\,^1\Sigma^+$), the 1NG CO^+ ($B\,^2\Sigma^+$

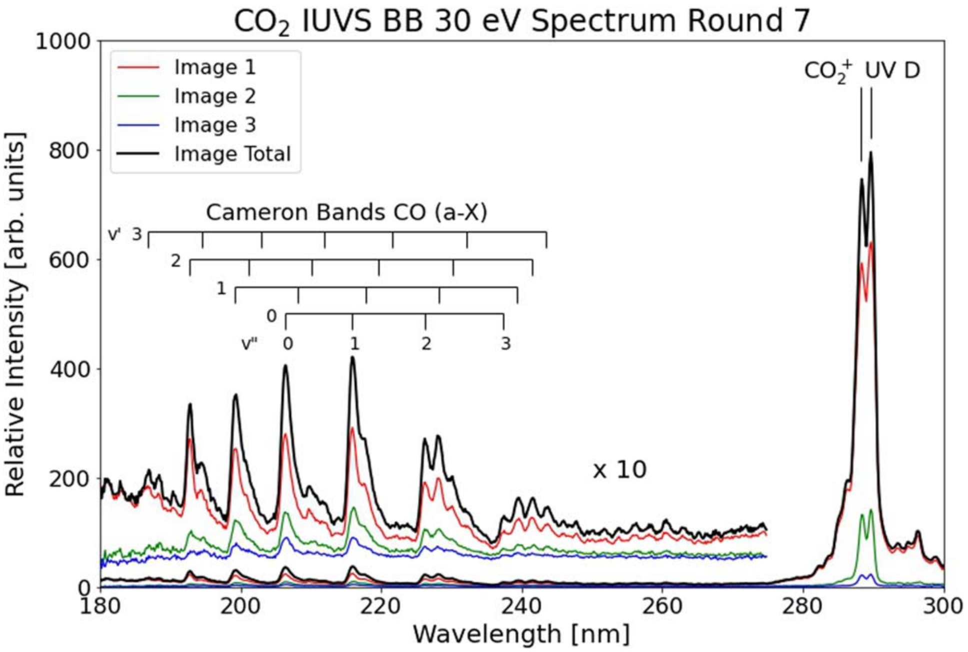

Figure 6. Calibrated MUV EIFS of e+CO_2 from 180–280 nm with CB identifications. The data show four sets of experimental spectra for the three image positions as well as the sum of the three images at 30 eV. Image 1, Image 2, and Image 3 were taken with the IUVS-OEU optical axis vertically raised with respect to the electron beam at 0, 15.2, and 30.4 cm, respectively. The electron impact fluorescence spectra for the images are at a gas pressure of 2–2.5 × 10^{-5} Torr with an electron beam current of ∼80 μA.

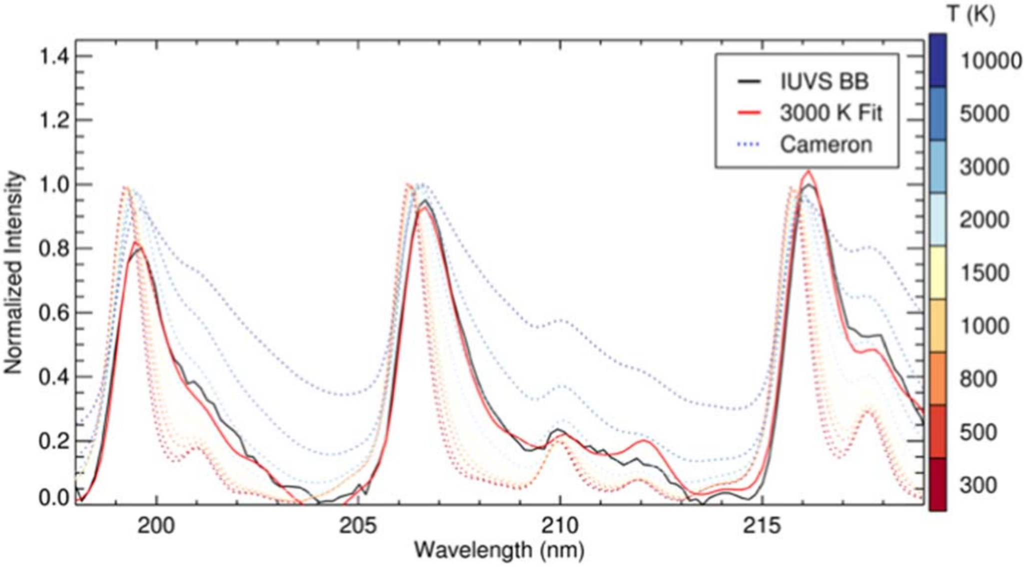

Figure 7. Optimal CB shape at a range of temperatures (indicated by the color bar) compared to the measurement for electron energy of 30 eV (black).

$\rightarrow X\,^2\Sigma$), and the CB CO ($a\,^3\Pi \rightarrow X\,^1\Sigma^+$) are the band systems of CO and CO^+ observed that are excited by CO_2 dissociative excitation and the CO_2^+ UVD ($\tilde{B}\ ^2\Sigma_u^+ \rightarrow \tilde{X}\ ^2\Pi_g$, at 288.3 and 289.6 nm); and (2) atomic features from electron excitation (Ajello 1971a; Ajello et al. 2019). The CB emission arising from the $a\,^3\Pi$ state can be strongly populated by cascade, in addition to direct dissociative excitation, from the optically allowed cascading from a host of triplet states with excitation energies above the threshold at 6.01 eV for the *a*-state as shown in the energy level diagram in Figure 1 of Lee et al. (2021). This process has been found to be the dominant excitation process contributing to the CB emission cross section at 15 eV from CO gas (Lee et al. 2021). The strongest cascade process arises from the $d\ ^3\Delta$ and $a'\ ^3\Sigma^+$ electronic states.

When a CO_2 molecule is excited by a low energy electron above 12 eV the following reactions will energetically occur as Judge & Lee (1973) measured in a corresponding photodissociation experiment:

$$CO_2 + h\nu(\varepsilon <\ 12\ \text{eV})\ \rightarrow\ CO_2^*$$
$$\rightarrow CO(a\ ^3\Pi,\, a'\ ^3\Sigma^+,\, d\ ^3\Delta,\, e\ ^3\Sigma^- + O\ (^3P). \qquad (2)$$

The excited CO molecules formed in those triplet states, exclusive of the state, $aa'\ ^3\Pi$ will then cascade into the $a\,^3\Pi$ state through dipole-allowed radiative decay

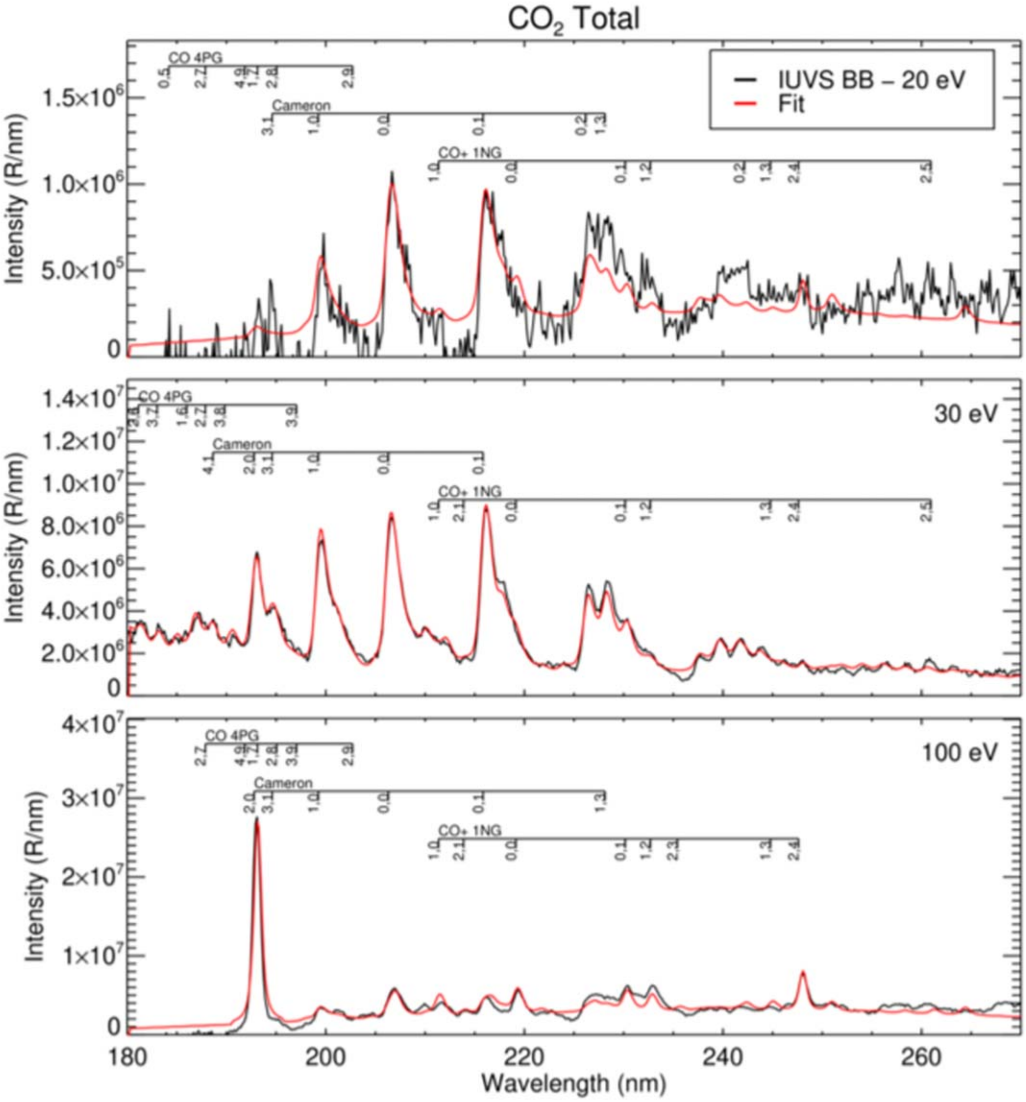

Figure 8. Measured electron-impact-fluorescence MUV spectra (black) from a CO$_2$ gas for (top) 20 eV, (middle) 30 eV, and (bottom) 100 eV electrons compared with MLR fits (red) from the 4PG, 1NG, and CB model vectors.

(Judge & Lee 1973), i.e.,

$$\mathrm{CO}\ (a'\ ^3\Sigma^+,\ d\ ^3\Delta,\ e\ ^3\Sigma^-)\ \rightarrow\ \mathrm{CO}\ (a\ ^3\Pi) + h\nu_{\mathrm{vis-IR}}. \qquad (3)$$

These emissions have been detected by Cook et al. (1966) as part of a CO$_2$ EUV absorption experiment using a glass filter. In our case for electrons, in a similar way,

$$\mathrm{CO_2}\ (\tilde{X}\ ^1\Sigma_g^+) + e\ \rightarrow\ \mathrm{CO_2^*}\ (\text{singlets, triplets}) + e$$

$$\mathrm{CO_2^*}\ \rightarrow\ \mathrm{CO}(a'\ ^3\Sigma^+,\ d\ ^3\Delta,\ e\ ^3\Sigma^-) + \mathrm{O}\ (^3P,^1D), \qquad (4)$$

$$\mathrm{CO}(a'\ ^3\Sigma^+,\ d\ ^3\Delta,\ e\ ^3\Sigma^-)\ \rightarrow\ \mathrm{CO}\ (a\ ^3\Pi) + h\nu_{\mathrm{vis-IR}}, \qquad (5)$$

followed by

$$\mathrm{CO}(a\ ^3\Pi)\ \rightarrow\ \mathrm{CO}(X\ ^1\Sigma^+) + h\nu_{\mathrm{CB}}. \qquad (6)$$

The enhanced MUV intensity CB spectra in the 20 eV electron impact fluorescence spectrum shown in Figure 1(a) from 240–280 nm, similar to that found by Erdman & Zipf (1983), is uncertain and may be due to cascade from these CO high-lying triplet states.

MLR model spectra (hereafter templates) were generated with the Atmospheric Ultraviolet Radiance Integrated Code (AURIC; Strickland et al. 1999; Evans et al. 2015; Stevens et al. 2015; Steffl et al. 2020). The model templates include electron impact dissociation of CO$_2$ producing CO 4PG bands (Kurucz 1976; Durrance 1980; Ajello et al. 2019; Lee et al. 2021), CO CBs (Conway 1981; Stevens et al. 2019), dissociative ionization of CO$_2$ producing CO$^+$ 1NG bands (Conway 1981; Stevens et al. 2019), and ionization of CO$_2$ producing the CO$_2^+$ UVD (Farley & Cattolica 1996). The atomic carbon sources C I 193.1, N III 218.8, C III 216.3, C I 247.8, N II 282.3, C II 283.7, C I 296.5, and C I 296.7 nm were included as delta functions run through a simulator of the IUVS instrument, with centers and relative line strengths provided by the NIST Atomic Spectra Database (Kramida et al. 2018). The IUVS flight and BB sensitivity curve (McClintock et al. 2015) was applied to all templates to perform MLR fits in count space and to calibrate the resulting model fit into physical units. All templates were shifted to the red by 0.07 nm to best align sources with their appearance in the measured spectra. The data were also constrained to 180–300 nm to avoid the CO$_2^+$ FDB bands at higher wavelengths. All templates were then combined as a regression matrix and binned onto the

Table 1
CO CB Relative Vibrational Populations Normalized to Unity

v'	Conway (1981)	This Work
0	0.36	0.37 ± 0.02
1	0.27	0.26 ± 0.01
2	0.16	0.17 ± 0.04
3	0.06	0.05 ± 0.02
4	0.06	0.04 ± 0.02
5	0.04	0.04 ± 0.02
6	0.02	0.04 ± 0.02
7	0.03	0.03 ± 0.03

Table 2
CO^+ 1NG Relative Vibrational Populations Normalized to Unity at $v' = 1$

v'	Conway (1981)	This Work
0	0.81	0.41 ± 0.09
1	1.00	1.00 ± 0.14
2	0.79	1.72 ± 0.66
3	⋯	15.83 ± 2.55
4	⋯	81.39 ± 10.67
5	⋯	134.77 ± 45.39

Table 3
CB and UVD Electronic Emission Cross Section Comparisons (Avakyan et al. (1998)[a] and This Work)

Energy (eV)	Emission Cross Section (10^{-17} cm^2)				
	UVD Image 1 Direct[a]	UVD Total	% UVD Long-lived	CB Total	CB Total[a]
11.46	⋯	⋯	⋯	AP	AP
16	⋯	⋯	⋯	3.2	4.2
20	0.7	1.00	29.2	4.43	14.4
30	1.8	2.17	16.9	0.99	20.4
40	2.6	3.07	15.3	0.56	22.0
50	3.1	3.77	17.7	0.48	23.0
100	4.6	5.58	17.5	0.35	24.0

Notes. The 16 eV cross section value of 3.2×10^{-17} cm^2 for our work is based on fitting the excitation function of Freund (1971)'s Figure 5 normalized to our peak cross section value of 4.43×10^{-17} cm^2 at 20 eV. AP = appearance potential (Avakyan et al. 1998).

[a] From Avakyan et al. (1998).

measurement wavelength grid. A bound value least-squares regression routine (Cappellari 2017) was used to determine fit coefficients for each template against each measurement, constraining all coefficients to be nonnegative.

By utilizing AURIC band models for the regression, we are able to create templates for each upper vibrational level for each band system. Creating templates with upper-level vibrational intensities normalized to unity allows the regression to determine optimal upper-level vibrational populations. This was done for both the CB and 1NG band systems. The resulting CB populations averaged across all energies are compared to those derived by Conway (1981) in Table 1. Resulting populations for the first three vibrational levels of the 1NG fit are compared to values derived by Conway (1981) in Table 2; higher vibrational levels were insignificant to any fits. Uncertainties for the relative vibration populations presented in Tables 1 and 2 are derived from a sum-squared combination of the random uncertainties for both light and dark frames corresponding to Images 1, 2, and 3. This spectral uncertainty is propagated through IDL's regress procedure to determine uncertainties corresponding to the resultant population coefficients. These uncertainties are scaled as necessary with the normalization used on their respective relative vibrational populations.

Cross sections from 30–100 eV (see Table 3) were determined by combining the two separate fits and referencing an established cross-sectional standard for UVD (Avakyan et al. 1998) for Image 1 (assumed as only measured previously in a small collision chamber). The total cross sections for the FDB bands CO_2 ($\tilde{A}\ ^2\Pi_u \rightarrow \tilde{X}\ ^2\Pi_g$, 280–500 nm), from a set of measurements conducted in a small chamber, are also given in Avakyan et al. (1998). For comparison, the 20 eV emission cross section of UVD from Avakyan is 0.7×10^{-17} cm^2 and the total emission cross section of the FDB bands is 0.9×10^{-17} cm^2. The emission cross sections of the FDB bands over the wavelength range 293–470 nm are fully measured and discussed in Ajello (1971b) and are not remeasured in this MUV study due to the limited range of MUV wavelengths discussed herein. The initial vibronic populations of the $\tilde{A}$ and $\tilde{B}$ states are perturbed by their proximity to one another (Samson & Gardner 1973 for the $\tilde{B}$ state). Moreover, the $\tilde{C}\ ^2\Sigma_g^+$ ionic state would be expected to cascade into the $\tilde{A}$ and $\tilde{B}$ states.

The quality of the MLR fit to the 20 eV spectrum in Figures 8 and 9 did not meet the same standard of correlation coefficient. The correlation coefficient was 0.74 for the 20 eV spectral model whereas all the other energies from 30–100 eV produced a correlation coefficient above 0.95. Furthermore, the signal-to-noise ratio was decidedly less in the 20 eV spectrum. Thus, the cross section at 20 eV was determined directly from the measured spectrum by comparing areas of the CB relative to UVD.

The total UVD cross section at 20 eV was scaled upward by 1.29 to account for cascade perturbation effects not measured previously (Ajello 1971a). The upward scaling of total UVD cross sections at energies from 30–100 eV is given in percent in Column 4 of Table 3 and is nominally 15–18%. By measuring a relative intensity from the UVD model fit for Image 1, to a relative intensity from the CB model fit, and propagating the UVD standard through the ratio of the two, a CB cross section was obtained. The resulting CB cross section was scaled by 1.78 to account for wall drift effects for a fast 1 eV CO ($a\ ^3\Pi$) dissociation product with a 3 ms lifetime, estimated through fitting and extrapolating the radial glow patterns and high spectral resolution studies of CO dissociation into excited O (^{1}D) (LeClair & McConkey 1994; Beegle et al. 1999).

Figure 8 highlights the quality of fit as well as major band contributions from 4PG, 1NG, and CB for 20, 30, and 100 eV

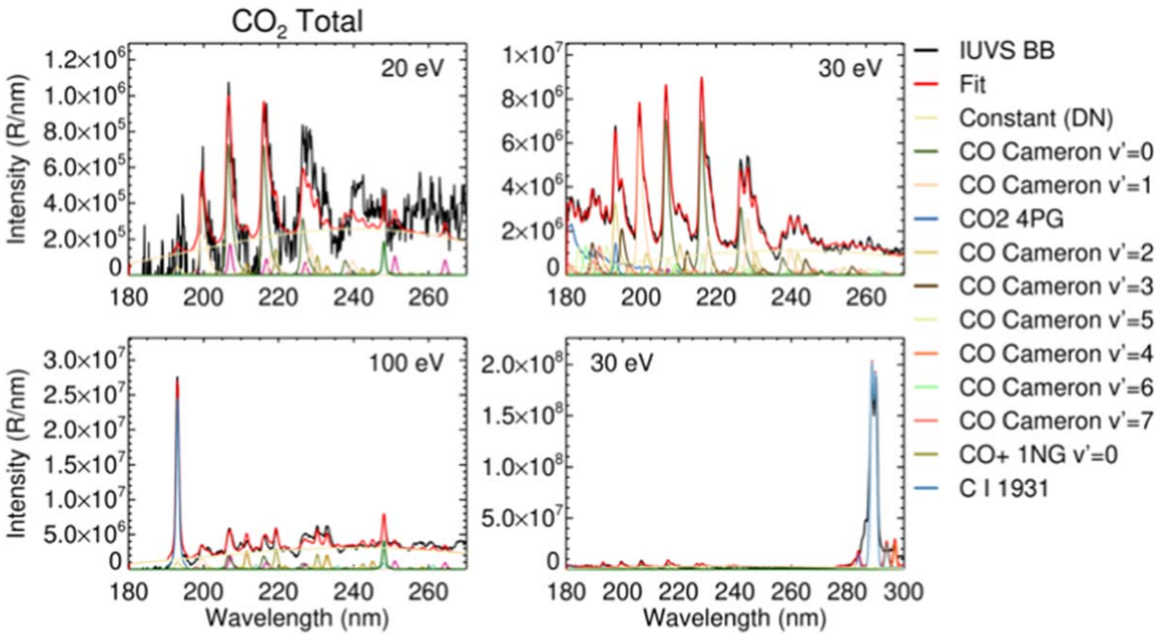

Figure 9. Measured electron-impact-fluorescence MUV spectra (black) from a CO_2 gas for upper left: 20 eV, upper right: 30 eV, and bottom left: 100 eV electrons compared with MLR fits (red) from the 4PG, 1NG and CB model vectors. The individual fit components are listed in the legend in order of total contribution across the shown wavelength range. The bottom right panel extends the observed range to include the UVD source at 30 eV.

measurements. Figure 9 illustrates the fit by constituent sources. The order of items in the legend indicates the total intensity contribution to the fit over the shown wavelengths. Figure 9 shows a representative fit including the UVD source to highlight how much it dominates the spectra for every observed energy level, and why a combination of two fits was necessary.

5. Electronic Emission Cross Sections

We have measured the emission cross section of the CB in the MUV over the wavelength range from 180–280 nm as well as the UVD over the wavelength range from (278–291 nm) from the electron impact process e+CO_2, with excitation thresholds for the $a\,^3\Pi$ state at 11.5 eV and UVD at 18.1 eV, at five electron impact energies: 20, 30, 40, 50, and 100 eV. For each of the data sets the background subtraction of the raw MUV spectra was determined from the 21 spectral wavelength pixels from 333.0–336.3 nm. This wavelength region presents no significant FDB molecular band contribution, as shown in the raw spectrum illustrated in Figure 5 for 50 eV. The CB wavelength range for emission cross section determination for the five electron energies from 20–100 eV was measured from 182.5–280.7 nm. Conway (1981) indicates no significant contribution to CB below 182.5 nm nor above 280 nm (see Figure 1). The CB and UVD emission cross sections are given in Table 3 in comparison to the previous emission cross section review by Avakyan et al. (1998). We show in Figure 10 a comparison to the peak cross sections of Freund (1971) normalized at 27 eV to their published peak value of 4×10^{-17} cm^2. LeClair & McConkey (1994) published a value of 2.4×10^{-16} cm^2, normalized to the 80 eV excitation cross section of Erdman & Zipf (1983) with a value of 2.8×10^{-16} cm^2. We show in Figure 10 the excitation function of LeClair & McConkey (1994) normalized at 22 eV, the peak excitation function energy, to the corresponding peak excitation energy of 4×10^{-17} cm^2 of Freund (1971). These two experiments were a time of flight (TOF) and were designed mainly for detecting slow CO ($a\,^3\Pi$) fragments from direct excitation and allowed (fast) cascading.

Cascade fragments are identified by bumps in the measured TOF excitation functions. The 20 eV emission cross section measured in this work shows excellent agreement with those TOF studies from the literature (Freund 1971; LeClair & McConkey 1994). However, there are many dissociating and predissociating states that can contribute to each type of excitation function in Figure 10 for both the emission and TOF experiments. The excitation functions measured in the TOF experiments are sensitive to whether the main process is either direct excitation or cascading (allowed or optically forbidden) from high-lying triplet states. There are multiple pathways to arrive at the CO ($a\,^3\Pi$) state at each energy. The CO ($a\,^3\Pi$) state production can arise by either a dissociation or predissociation process as indicated in Figure 4. The slow CO ($a\,^3\Pi$) molecular fragments have typical kinetic energy of 0.5–2 eV in the TOF studies of Freund (1971) as we found (Beegle et al. 1999) from high-resolution atomic line profile studies. Freund points out that anisotropy of fragments can occur in the case of predissociation. We also note the TOF excitation function of Freund in Figure 10 from 30–100 eV electron excitation energy has the same shape as our excitation function from 30–100 eV. However, uncertainties such as detector efficiency in TOF measurements indicate an order-of-magnitude uncertainly in the TOF absolute cross sections.

We show in Figure 10(b) an analytical fit to the CB CO ($a\,^3\Pi \rightarrow X\,^1\Sigma^+$) emission cross section as a function of energy using the Freund cross section values normalized to the value in Table 3 at 20 eV. We used Equation (3) from Shirai et al. (2001) to fit the cross section since that is the expression they used to fit the e+CO CB emission cross section, which has a similar shape. The fit coefficients for a threshold energy of 11.46 eV are: [2.16e+01, 5.68e+00, 6.47e-03, 3.72e-01, −1.15e+00, 2.03e+00, 1.13e+00, 3.84e-01] with parameter uncertainties of approximately 30%. See also Zubek et al. (1997). The emission cross section shape of the $b\,^3\Sigma^+ \rightarrow a\,^3\Pi$

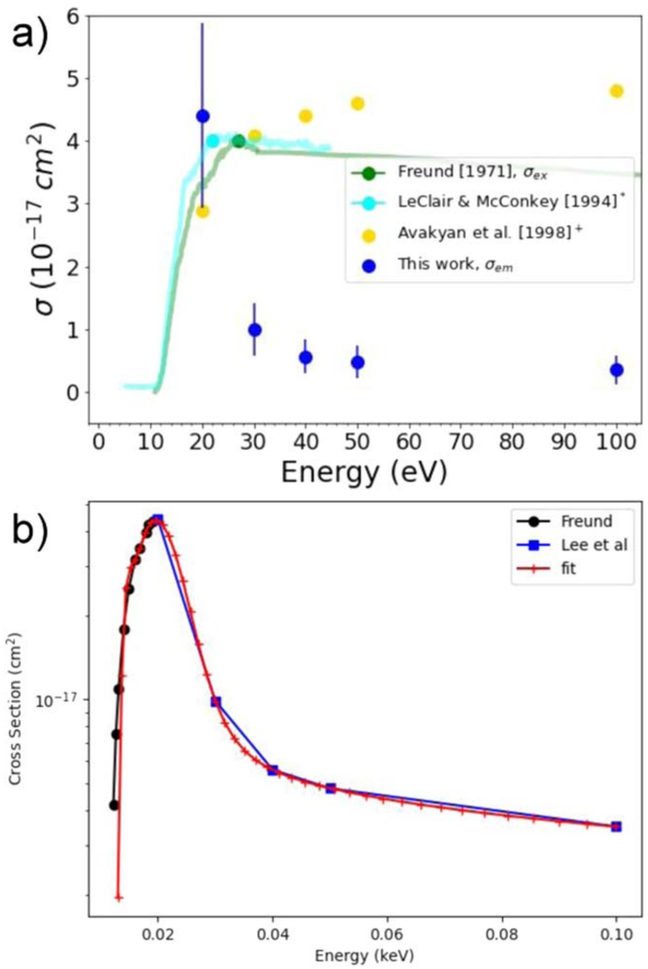

Figure 10. (a) CB CO ($a\,^3\Pi \rightarrow X\,^1\Sigma^+$) emission cross section as a function of energy from e+CO_2 shown in blue dots of this experiment (Table 3) with uncertainty bars of 35% (Lee et al. 2021). We show a comparison of the emission function of this experiment to the excitation cross-sectional measurements of Freund (1971) in green, LeClair & McConkey (1994) in blue, and Avakyan et al. (1998) in yellow. A * indicates the solid point in light blue is the peak excitation function measurement of LeClair and McConkey normalized to the excitation function of Freund. A + sign indicates values have been divided by a factor of 5. (b) An analytical fit to the CB CO ($a\,^3\Pi \rightarrow X\,^1\Sigma^+$) emission cross section as a function of energy using Freund cross section values normalized to the value in Table 3 at 20 eV.

band system from the state for CO shown in Itikawa (2002)'s Figure 11 and Table 8 is the same as what we find for the overall $a - \tilde{X}$ emission cross section for e+CO_2 (Figure 10(b)).

Samson & Gardner (1973) studied photoionization of CO_2 by He I (58.4 nm) that produces ions in the $\tilde{X}\,^2\Pi_g$, $\tilde{A}\,^2\Pi_u$, $\tilde{B}\,^2\Sigma_u^+$, and $\tilde{C}\,^2\Sigma_g^+$ electronic states. The $\tilde{C}$-state is fully predissociated into CO ($X\,^1\Sigma^+$) + O^+ (^4S) at threshold (19.4 eV) electron energy upon electron bombardment. Samson & Gardner (1973) also studied photoionization by He II 30.4 and found the production of CO ($a\,^3\Pi$) spontaneous radiation lifetime is slightly longer than that of the $\tilde{A}$-state (118 versus 113 ns). A more substantial radiative lifetime difference was found by Schlag et al. (1977) using electron-photon coincidence measurements of 120 versus 100 ns.

Several authors discuss the vibrational levels causing the inter-electronic coupling between the $\tilde{A}$ and $\tilde{B}$-states (e.g., Leach et al. 1978; Tokue et al. 1990). We see in our spectra (Figure 6) that the effect of the coupling causes long-lived emission from the $\tilde{A}$ and $\tilde{B}$ states at a 15%–30% branching ratio (see Table 3), responsible for the $\tilde{B}$-state off-axis emission occurring in Images 2 and 3. Our experiment finds the same effect in the $\tilde{A}$-state molecular emission from vibronic emissions near the UVD within the wavelength range of 300–320 nm. This is the first experiment to provide evidence of both $\tilde{A}$-state and $\tilde{B}$-state perturbed vibronic emissions.

The emission cross section results in Table 3 and Figure 10 represent a major change to the previous CB cross sections of Avakyan et al. (1998) and the shape of the excitation function. This change indicates a peak CB emission cross section in the optically forbidden emission from two equally probable processes for a polyatomic molecule: predissociation or dissociation. The peak emission cross section occurs in the range of 11.5 eV (threshold energy) to 30 eV (a value in energy near the peak electron energy indicated by TOF studies; Figure 10). Although TOF absolute excitation function measurements are greatly uncertain, we find a verification of the CB MUV emission cross sections presented in Table 3. Freund (1971) finds the peak cross section for the formation of CO ($a\,^3\Pi$) is 4×10^{-17} cm^2 at 27 eV, compared to our value of 4.43×10^{-17} cm^2 at 20 eV, a value near the peak energy. The measured 20 eV emission cross section is the average from six images. LeClair & McConkey (1994) in another TOF experiment, using solid Xe as a metastable detector observed a cross-sectional peak at 22 eV. An excitation function similar in shape to that of Freund (1971) was measured by LeClair & McConkey (1994).

LeClair & McConkey (1994) note that the rapid rise to the maximum of the excitation function for the CB indicates the prominent role played by a spin-flip transition to the dissociating parent state. The gradual falloff after the peak at 22 eV for the TOF studies has been reached shows contributions from both excited triplet and singlet states after excitation of CO_2 ($\tilde{X}\,^1\Sigma_g^+$) ground state into a predissociating excited state, as shown schematically in Figure 4 and Equations (4)–(6). Our excitation function indicates a sharp falloff after the peak energy, indicating the importance of singlet-triplet transition(s). We show the Freund excitation function in Figure 10 in the threshold region for energies below its peak value at 27 eV. We note that Freund did not discuss the significant contribution to cascading (Equation (7) and Equation (8)) to the a-state absolute excitation cross section from high-lying electronic states following dissociative or predissociative excitation of CO_2. Structure in the CO ($a\,^3\Pi$) TOF excitation function studies coincides with the high-lying electronic states of CO at their low energy electron impact thresholds:

$$\mathrm{CO}(a'\,^3\Sigma^+,\ d\,^3\Delta) \rightarrow \mathrm{CO}(a\,^3\Pi) + h\nu_{\mathrm{vis-IR}} \qquad (7)$$

followed by

$$\mathrm{CO}(a\,^3\Pi) \rightarrow \mathrm{CO}(X\,^1\Sigma^+) + h\nu_{\mathrm{CB}}. \qquad (8)$$

The published estimated error in the Freund absolute cross section is an order of magnitude, but the excitation function shape is correct to ~15%. The threshold excitation function shape of Freund in Figure 10 can be used as a threshold estimate of the CB emission cross section from 11.5–20 eV.

The value given by Itikawa (2002) in a cross-sectional review paper is the value of Erdman & Zipf (1983) of 2.4×10^{-16} cm^2, which relies on the original work of Ajello (1971b). The review acknowledged the CB cross section to be in error by at least a factor of 2, and moreover, it acknowledged

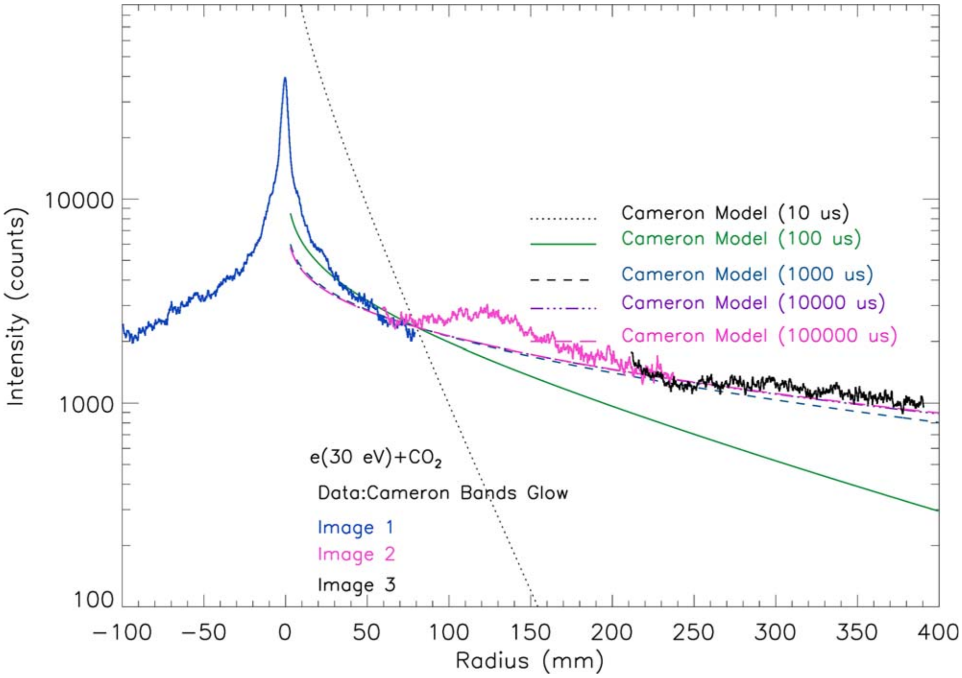

Figure 11. The observed glow profile of the CB. The radial glow pattern extends from the beam center at 0–400 mm. The CB glow pattern (integrated line-of-sight intensity vs. radius) imaged by the IUVS-OEU across the diameter of MOBI from electron excitation CO_2 gas is a function of two variables: (1) the dipole-forbidden lifetime of the CO ($a\ ^3\Pi$) atom and (2) the mean kinetic energy for fragmented CO ($a\ ^3\Pi$) exited molecule. The radial line-of-sight intensity dependence with respect to the minimum ray height radial distance can be approximated by a single exponential function dependence on the product of mean kinetic energy and lifetime as shown in Equation (1) of Ajello et al. (2017). We show the model regression fits for a range of lifetimes in color for each glow based on our previously measured lifetime for 3 ms. The glow profile model with a single lifetime is an approximation to a complicated process involving disassociation and predissociation from an array of singlet and triplet states of CO_2 as described earlier. A more reliable and simple single lifetime glow pattern yielding a more accurate lifetime for the CB is shown in Figure 8 in Lee et al. (2021).

CB cross sections to be unreliable at the present time. More importantly, the variation in the two sets (our study and Avakyan et al. 1998) of emission cross sections in Table 3 changes from near a factor of 4 at 20 eV to 71 at 100 eV. We intend to study the important electron impact low energy region from threshold to 20 eV in the near future by observing CB emission.

6. CB Glow Profile

The distance a CO ($a\ ^3\Pi$) molecule will travel before radiating depends on its lifetime and kinetic energy after dissociation. The CB volume emission rate in the cylindrical glow about the electron beam falls off a little faster than r^{-1} (where r is the radius of the glow about the electron beam), due to the exponential factor with lifetime (Ajello et al. 2017). The triplet states energetically above the *a*-state (see Figure 1 in Lee et al. 2021) all radiate promptly to the $a\ ^3\Pi$ state with a lifetime of the order of a few microseconds (Strobl & Vidal 1987). We have shown that a measurement of the glow profile at room temperature is a measure of the lifetime and kinetic energy of the CO ($a\ ^3\Pi$) excited molecule as gauged in excess kinetic energy with respect to the dissociation limit (Ajello et al. 2017, 2019). The extent of the CO_2 glow is larger with a longer lifetime and the higher the kinetic velocity of dissociation above (first) dissociation limit of 5.45 eV + 6.01 eV ($v' = 0$ excitation energy) to CO ($a\ ^3\Pi$) excitation energy to CO ($a\ ^3\Pi$) with a value of 11.46 eV. In the present work, the IUVS instrument was placed on a vertical moving stage with the entrance slit orthogonal to the electron beam. The $1/e$ distance traveled before radiating for a thermal 39 meV excited CO ($a\ ^3\Pi$) molecule is 155 cm as for the case of excitation of the CB from CO whereas the CO_2 molecule is excited first to a repulsive curve as shown in Figure 4 and the ∼1 eV kinetic energy for the excited CO ($a\ ^3\Pi$) molecule provides a $1/e$ travel distance of ∼785 cm.

Figure 11 shows the full glow concatenated pattern of the CB from 180–280 nm at 30 eV for the three images staged across the 0.75 m radius of MOBI from electron impact fluorescence over the range of CO ($a\ ^3\Pi$) state lifetimes from 10 μs to 0.1 s (see Lee et al. 2021). We can model the CB glow as a function of the minimum ray height radius from the electron beam to the line of sight. The model in Figure 11 indicates a best fit for a lifetime of ∼3 ms. The difference between a finite chamber of 0.75 m radius and a 5 m chamber in line-of-sight column emission amounts to only an extra 6% loss along the line of sight. We account for this loss of signal in our cross-sectional calculations. The best fit model for the direct-excitation lifetimes in either case is 3 ms with an uncertainty of 1 ms. Thus, the CO ($a\ ^3\Pi$) lifetime is $\sim 3 \pm 1$ ms.

Figure 12 shows the full glow concatenated pattern of the CB for the three images staged across the 0.75 m radius of MOBI from electron impact fluorescence at 20 eV impact energy of the parent gas CO_2. Figure 12 also shows the UVD at 20 eV and for comparison the C I (193.1 nm) atomic electron impact fluorescence also at 100 eV. With a dipole-allowed lifetime of 3 ns the C I (193.1 nm) emission occurs on the electron axis and maps the breadth of the electron beam with electrostatic focusing of the 0.3 m length of the electron beam as 20–25 mm FWHM at the central point of the long electron beam. The C I ($^1P^o \rightarrow {}^1D$) 193.1 nm signal, with a lifetime of 3 ns and minor contributions from both allowed and forbidden

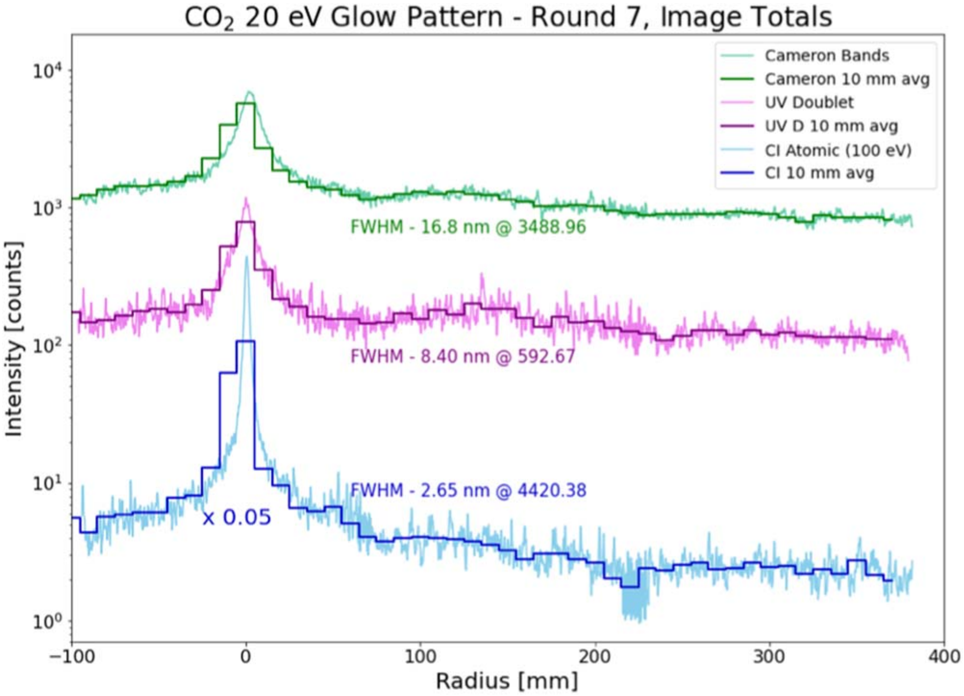

Figure 12. Observed glow profile of three features in the second order MUV spectrum of e(20eV)+CO_2. The radial glow pattern extends from the beam center at 0–400 mm. We indicate glow profiles for three emission features: the CB from 180–270 nm, the UVD, and the C I 193.1 nm atomic multiplet. The C I 193.1 profile has been reduced by a factor of 20 to better compare the profile shapes.

cascading states, drops by 2 orders of magnitude and the UVD and CB signals both drop by an order of magnitude due to the secondary processes of cascade and inter-electronic perturbations.

Additionally, Figure 12 shows the normalized peak intensity signal in counts of the line-of-sight integrated emission intensities for the UVD, CB, and C I (193.1 nm) features, respectively, as a function of minimum ray height (radius) from the electron beam. The radial glow patterns for CO ($a\,^3\Pi$) need to be modeled using two types of slow emission processes (long metastable lifetime and fast kinetic energy of fragment O ($^3P^o$) atom) with distance from the electron beam as shown in Figures 6 and 11. The lifetime of metastable CB is known to be 3 ms (Lee et al. 2021) and the ∼1 eV kinetic energy of the CO a-state molecule can experience a drift of the order of 800 mm before it undergoes radiative decay. CO_2^+ UVD ($\tilde{B}$-state) molecules can also experience a large drift before undergoing radiative decay due to the perturbed bi-exponential lifetime. This arises from a combination of the ∼120 ns short radiative lifetime for Image 1 and the perturbed lifetime from $\tilde{A}$–$\tilde{B}$ interelectronic coupling. The interelectronic coupling is produced from unresolved rovibrational emission lines in the low-resolution spectral experiment employed here. Another high-resolution spectral technique we have employed in the past is the study of the broadening of FUV atomic line profiles during dissociation of CO. The CO dissociates into fast atomic fragments with UV emission of transitions and line widths typically revealing mean kinetic energies of broadened dipole-allowed electronic states to be about ∼1 eV (Beegle et al. 1999).

7. Discussion and Summary

Based on recent laboratory needs expressed in the literature on planetary atmospheres (Simon et al. 2009) we have measured two of the most important UV emission cross sections required for forward modeling the electron excitation processes on Mars and Venus. Our unique laboratory measurements in a large vacuum chamber allow us to simultaneously study both allowed and dipole-forbidden or dipole-perturbed processes in a planetary atmosphere. For the case of Mars and Venus, we have studied processes leading to CB emission from both CO (Lee et al. 2021) and CO_2 (this work). We compare in Figure 13 the low (30 eV) energy laboratory MUV spectra from 180–265 nm for Images 1, 2, and 3 and the total sum for both CO (top) and CO_2 (bottom) and one IUVS dayglow observation at 150 km. The difference between the low energy CB electron-excited laboratory spectra for the two gases is apparent at 30 eV, an energy near the photoelectron mean energy. The CB UV emission from CO has a strong MUV contribution from the 4PG that blends with the CB strongly from 180–200 nm (Lee et al. 2021). On the other hand, the 4PG bands make a minor contribution to the CB production from CO_2 (see Figure 9). The vibrational intensity variations (v' = constant − v''-progressions) as indicated in Figure 13 are different for each gas, with progression upper and lower vibrational level tick marks shown above the experimental CO and CO_2 molecular spectra. In the laboratory, CO gas is at a room temperature of 300 K (0.039 eV mean kinetic temperature) in a gas swarm and 300 K is the rotational temperature. The CO_2 laboratory rotational temperature is modeled to be 4800 K (CO 4PG) from the profile of the rotational envelope. Both sets of CO and CO_2 laboratory spectra show strong evidence of the long lifetime of the CO ($a\,^3\Pi$) state with a strong contribution from Images 2 and 3.

As can be seen in Figure 14 the SPICAM MUV dayglow spectrum at its spectral low resolution of 1.5 nm (Bertaux et al. 2006) compared to a laboratory spectrum at a similar spectral resolution for e+CO_2 gas (30 eV). The match of the two

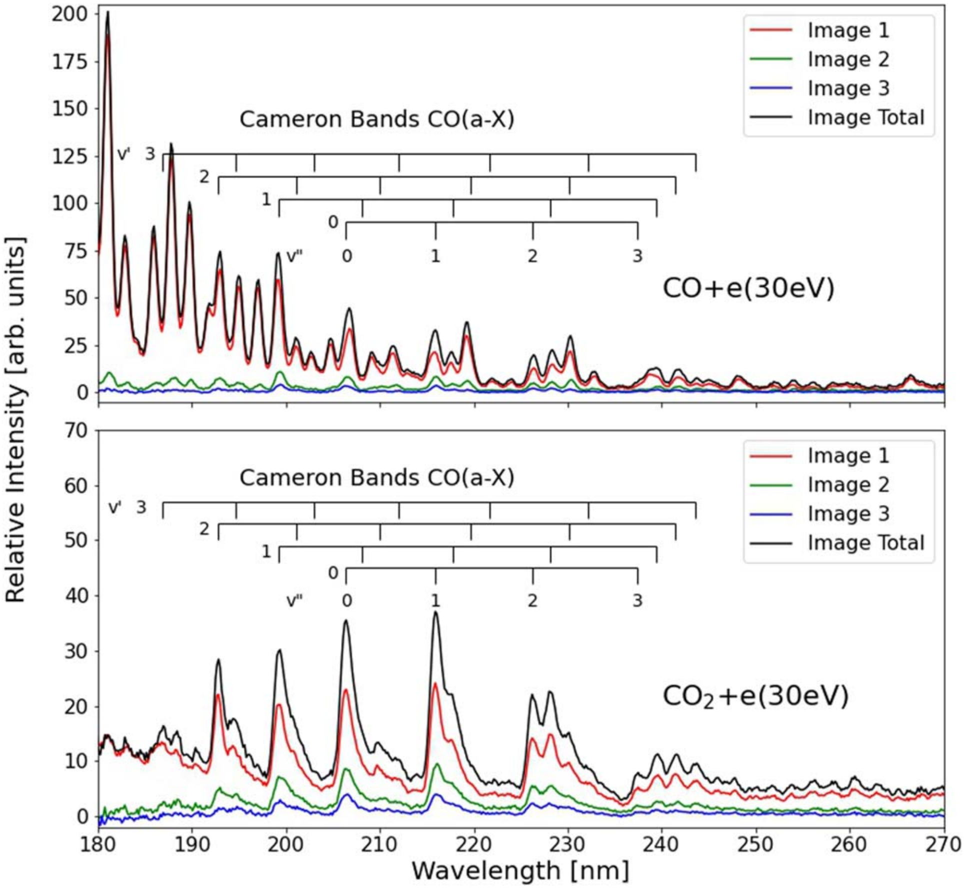

Figure 13. Top: calibrated MUV EIFS of CO between 180 and 270 nm. The data show four sets of experimental spectra for the three image positions plus the total at 30 eV. The IUVS-OEU optical axis in the vertical position with respect to the electron beam is nominally 0 cm (Image 1), 15.2 cm (Image 2), and 30.4 cm (Image 3). Bottom: calibrated MUV EIFS of CO_2 between 180 and 270 nm. The data show four sets of experimental spectra for the three image positions plus the total at 30 eV. The IUVS-OEU optical axis in the vertical position with respect to the electron beam is nominally 0 cm (Image 1), 15.2 cm (Image 2), and 30.4 cm (Image 3).

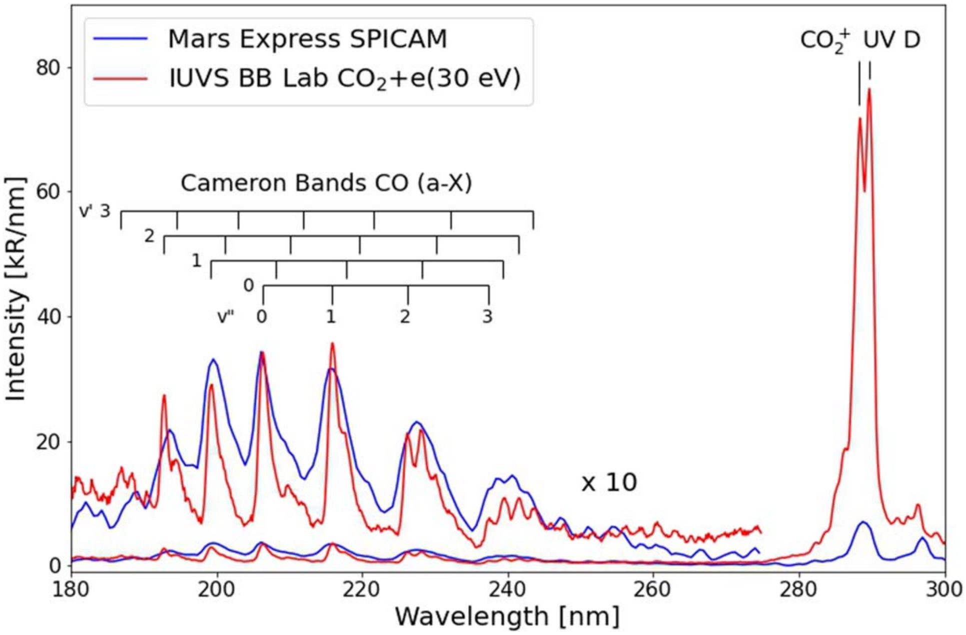

Figure 14. MUV lab spectrum of 30 eV $e^{-}+CO_2$ electron impact fluorescence using the IUVS flight spare compared to SPICAM dayglow observations, indicating the presence of CB bands and UVD.

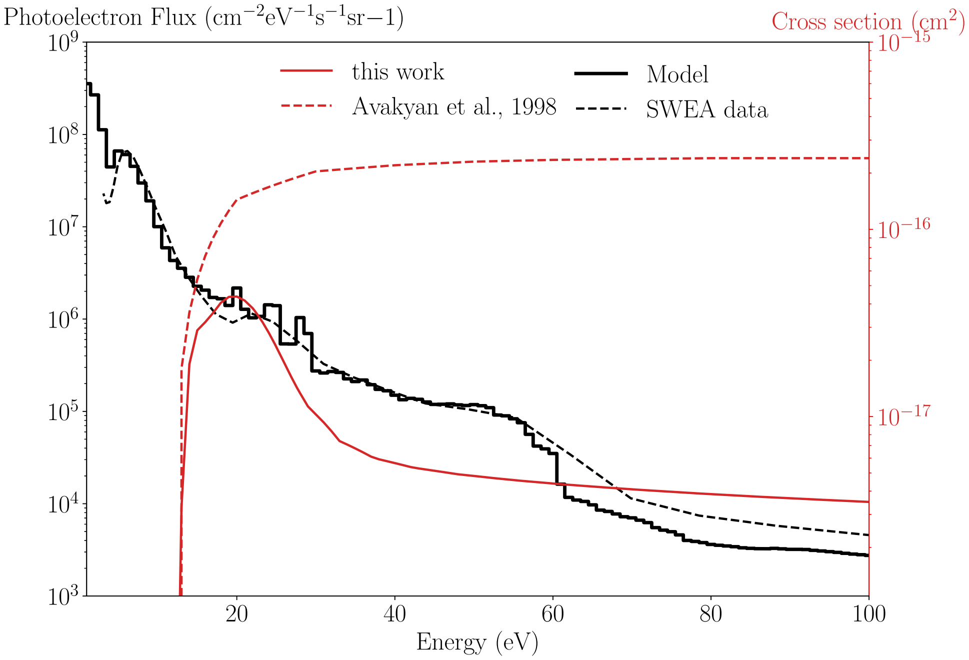

Figure 15. Observed and calculated mean photoelectron flux in the Mars ionosphere near 130 km (from Figure 2) are shown in black together with emission cross sections from this work (red solid line) and from Avakyan et al. (1998) (red dotted line).

spectra is remarkable exhibiting strong CB. For both cases of IUVS and SPICAM observations of CB emission in the Mars dayglow and aurora, electron impact fluorescence from CO seems to be a minor contributor, as the rotational temperature appears nonthermal based on Figure 13. The dayglow photodissociative excitation of CO_2 into the CO a state is a major contributor to the CB excitation, which partly offsets the electron impact contribution. We find the CO peak emission cross section at 20 eV to be 1.6×10^{-17} cm^2 compared to 4.4×10^{-17} cm^2 for CO_2. We find the cross section of both gases at the mean photoelectron energy to be similar, so the density of CO_2 gas is at least a factor of 10 times higher than CO over the minimum ray heights of 100–200 km. Models suggest that at the ionosphere peak CO represents less than 1% of the total density (Yung & Demore 1999; Chaufray et al. 2012).

At 20 eV the ratio of CB to UVD MUV emission cross sections is found to be 4.4, whereas if we use the Avakyan et al. (1998) CB MUV emission cross section, the ratio is 14.4. In contrast, Shematovich et al. (2008) scaled the Cameron emission cross section to the peak value of 2.4×10^{-16} cm^2 at 80 eV based on the recommendation by Erdman & Zipf (1983) and obtained reasonable agreement with limb profiles of the CB observed with SPICAM. Gérard et al. (2019) analyzed and modeled a set of CB and UVD dayglow limb profiles collected with the IUVS spectrograph. They obtained a good match with the observed CB limb spectra using a dayglow model using the same e+CO_2 cross section. However, other important sources of CO (a) state exist in the dayglow, such as processes (4) and (5) so that the total production rate of CO (a) will not decrease in the same proportion as the electron impact cross section, once the newly measured emission cross section is adopted.

The revision of the shape and decreased peak value of this dissociative excitation emission cross section has consequences on the modeled production rate of the CO $a\,^3\Pi$ state and the intensity of the CB's dayglow. The importance of this change is illustrated in Figure 15 showing the measured and modeled photoelectron flux on the Mars dayside together with the CO_2 dissociative excitation cross section from this work and from Avakyan et al. (1998). The model to calculate the steady state photoelectron energy distribution and CBs production rate were described by Jain & Bhardwaj (2012). The production rate of the CBs is the integral from threshold to infinity of the electron flux times the cross section multiplied by the local CO_2 number density. Based on our calculated electron flux at 130 km for conditions similar to MAVEN observations (as shown in Figure 15), the Cameron production rate drops by a factor of 5 from 2.7×10^3 to 5.4×10^2 cm^{-3} s^{-1} with current cross sections compared to ones calculated using Avakyan et al. (1998).

Soret et al. (2021) analyzed the composition of a total of 1452 IUVS limb spectra of discrete aurora, spread over 192 limb scans and 66 orbits. They found that the CB and UVD show maximum intensity at the same altitude. The mean value of the CB/UVD ratio was 6.6 ± 0.1. This value is within the range of the mean auroral ratios of 4.9 at the nadir (Gérard et al. 2015) and 9.0 at the limb (Soret et al. 2016) derived from SPICAM on board Mars Express. The aurora offers the characteristics relative to the dayglow that the only sources of CB auroral emission are processes (a), (b), and (d), whereas (c) plays a major role in the dayglow. Soret et al. (2016) modeled the expected brightness of the CB bands based on the electron energy spectrum measured in situ concurrently with the ASPERA-3 detectors on board Mars Express. The observed nadir CB brightness was generally less than predicted in the Monte Carlo simulation. The decrease of the electron impact cross section on CO_2 would then likely bring the observations into better agreement with the calculated intensities.

Although a detailed examination of the total production of the $a\,^3\Pi$ state in the dayglow is beyond the scope of this study, it is however interesting to note three important aspects. First, the new measurements presented in this study indicate that, in addition to the reduced peak value, the shape of the cross section is drastically modified so that the correction to

Avakyan et al.'s (1998) cross section is energy dependent. The decrease of the excitation cross section compared to Avakyan et al. reaches a large factor (up to 40) only at relatively high energies where the photoelectron flux is small. Therefore, it makes only a small contribution in comparison with energies closer to the peak of the revised cross section. Second, other processes such as photodissociative excitation of CO_2 and CO, photoelectron impact on CO, and dissociative recombination of CO_2^+ also contribute to the excitation of the CB production in the dayglow. For example, Jain & Bhardwaj (2012) and Gérard et al. (2019) showed that photodissociation of CO_2 is dominant above $\sim$160 km and is a significant source at the altitude of the emission peak. Therefore, the effect of the reduction of the electron impact source is mitigated by the presence of the other sources of the $a\,^3\Pi$ state. A third point, mentioned in the introduction, is that several models in the literature needed to empirically decrease the Avakyan et al. cross section to match the dayglow observations. Further detailed studies of the consequences of this revision will require additional detailed investigation.

This work was primarily performed at the Laboratory for Atmospheric and Space Physics (LASP), University of Colorado (CU) Boulder, and the Jet Propulsion Laboratory (JPL), California Institute of Technology (Caltech), under a contract with the National Aeronautics and Space Administration (NASA). We gratefully acknowledge financial support through NASA's Solar System Workings (SSW), and the National Science Foundation (NSF) GEO-AGS Aeronomy program, NSF award number 2031349. R.A.L. thanks the Boulder Solar Alliance NSF REU program for past support. J-C.G. is supported by the PRODEX program managed by the European Space Agency (ESA) with help from the Belgian Federal Science Policy Office (BELSPO). We thank Karl Hubbell for technical support and Bruce Jakosky, and the MAVEN team, for the usage of the IUVS Optical-Engineering Unit (OEU). U.S. government sponsorship is acknowledged.

ORCID iDs

Rena A. Lee https://orcid.org/0000-0001-7058-4134
Joseph M. Ajello https://orcid.org/0000-0002-5092-8494
Charles P. Malone https://orcid.org/0000-0001-8418-1539
J. Scott Evans https://orcid.org/0000-0003-2025-5695
Victoir Veibell https://orcid.org/0000-0001-9340-4503
Gregory M. Holsclaw https://orcid.org/0000-0002-9059-9437
William E. McClintock https://orcid.org/0000-0002-8142-5398
Sonal K. Jain https://orcid.org/0000-0002-1722-9392
Jean-Claude Gérard https://orcid.org/0000-0002-8565-8746
Saurav Aryal https://orcid.org/0000-0002-4919-1990
Nicholas M. Schneider https://orcid.org/0000-0001-6720-5519

References

Ajello, J. M. 1970, JChPh, 53, 1156
Ajello, J. M. 1971a, JChPh, 55, 3158
Ajello, J. M. 1971b, JChPh, 55, 3169
Ajello, J. M., Evans, J. S., Veibell, V., et al. 2020, JGRA, 125, e2019JA027546
Ajello, J. M., Malone, C. P., Evans, J. S., et al. 2019, JGRA, 124, 2954
Ajello, J. M., Malone, C. P., Holsclaw, G. M., et al. 2017, JGRA, 122, 6776
Al Matroushi, H., Lootah, F., Holsclaw, G., et al. 2019, in LPI Contribution 2089, Ninth Int. Conf. on Mars, 6073
Avakyan, S. V., Il'in, R. N., Lavrov, V. M., & Ogurtsov, G. N. 1998, in Collision Processes and Excitation of UV Emission from Planetary Atmospheric Gases: A Handbook of Cross Sections, ed. S. V. Avakyan (Amsterdam: Gordon and Breach)
Barth, C., Stewart, A., Hord, C., & Lane, A. 1972, Icar, 17, 457
Barth, C. A., Hord, C. W., Pearce, J. B., et al. 1971, JGR, 76, 2213
Barth, C. A., Hord, C. W., Stewart, A. I., et al. 1973, Sci, 179, 795
Beegle, L. W., Ajello, J. M., James, G. K., Dziczek, D., & Alvarez, M. 1999, A&A, 347, 375
Bertaux, J.-L., Korablev, O., Perrier, S., et al. 2006, JGRE, 111, E10S90
Budzien, S. A., Feldman, P. D., & Conway, R. R. 1994, JGR, 99, 23275
Cappellari, M. 2017, MNRAS, 466, 798
Cartwright, D. C. 1978, JGR, 83, 517
Chaufray, J.-Y., Bertaux, J.-L., & Leblanc, F. 2012, GeoRL, 39, 20
Conway, R. R. 1981, JGR, 86, 4767
Cook, G. R., Metzger, P. H., & Ogawa, M. 1966, JChPh, 44, 2935
Cox, C., Gérard, J.-C., Hubert, B., Bertaux, J.-L., & Bougher, S. W. 2010, JGRE, 115, E04010
Durrance, S. T. 1980, PhD thesis, Univ. Colorado Boulder
Eastes, R. W. 2000, JGR, 105, 18,557
Eastes, R. W., & Dentamaro, A. V. 1996, JGR, 101, 26931
Erdman, P. W., & Zipf, E. C. 1983, P&SS, 31, 317
Evans, J. S., Stevens, M. H., Lumpe, J. D., et al. 2015, GeoRL, 42, 9040
Farley, D. R., & Cattolica, R. J. 1996, JQSRT, 56, 83
Fox, J. L. 2008, JGRE, 113, E11001
Fox, J. L., & Dalgarno, A. 1979, JGR, 84, 7315
Fox, J. L., & Dalgarno, A. 1981, JGR, 86, 629
Freund, R. S. 1971, JChPh, 55, 3569
Gauyacq, D., Horani, M., Leach, S., & Rostas, J. 1975, CaJPh, 53, 2040
Gérard, J. C., Bougher, S. W., López-Valverde, M. A., et al. 2017, SSRv, 212, 1617
Gérard, J. C., Gkouvelis, L., Ritter, B., et al. 2019, JGRA, 124, 5816
Gérard, J. C., Soret, L., Libert, L., et al. 2015, JGRA, 120, 6749
González-Galindo, F., Chaufray, J. Y., Forget, F., et al. 2018, JGRE, 123, 1934
Gronoff, G., Simon Wedlund, C., Mertens, C. J., et al. 2012, JGRA, 117, A05309
Herzberg, G. 1950, Molecular Spectra and Molecular Structure: Spectra of Diatomic Molecules, Vol. 1 (New York: Van Nostrand Reinhold)
Herzberg, G. 1966, Molecular Spectra and Molecular Structure: Electronic Spectra of Polyatomic Molecules, Vol. 3 (New York: Van Nostrand Reinhold), 429
Herzberg, G. 1971, The Structure and Spectra of Simple Free Radicals (Ithaca, NY: Cornell Univ. Press.)
Holsclaw, G. M., Deighan, J., Almatroushi, H., et al. 2021, SSRv, 217, 79
Hubert, B., Gérard, J. C., Gustin, J., et al. 2010, Icar, 207, 549
Itikawa, Y. 2002, JPCRD, 31, 749
Jain, S. K., & Bhardwaj, A. 2012, P&SS, 63-64, 110
Jain, S. K., Stewart, A. I. F., Schneider, N. M., et al. 2015, GeoRL, 42, 9023
Jakosky, B. M., Lin, R. P., Grebowsky, J. M., et al. 2015, SSRv, 195, 3
Judge, D. L., & Lee, L. C. 1973, JChPh, 58, 104
Kanik, I., Noren, C., Makarov, O. P., et al. 2003, JGRE, 108, 5126
Kramida, A., Ralchenko, Y., Nave, G., & Reader, J. 2018, APS Meeting, 63, M01.004
Kurucz, R. L. 1976, The Fourth Positive System of Carbon Monoxide, SAO Special Report, #374
Lawrence, G. M. 1970, PhRvA, 2, 397
Lawrence, G. M. 1972, JChPh, 56, 3435
Leach, S., Stannard, P. R., & Gelbart, W. M. 1978, MolPh, 36, 1119
LeClair, L. R., & McConkey, J. W. 1994, JPhB, 27, 4039
Lee, R. A., Ajello, J. M., Malone, C. P., et al. 2021, JGRE, 126, e06602
Lefebvre-Brion, H., & Field, R. W. 2012, Perturbations in the Spectra of Diatomic Molecules (Orlando, FL: Elsevier) doi:10.1016/B978-0-12-442690-0.50005-1
Makarov, O. P., Kanik, I., & Ajello, J. M. 2003, JGRE, 108, 5125
McClintock, W. E., Schneider, N. M., Holsclaw, G. M., et al. 2015, SSRv, 195, 75
Mitchell, D. L., Mazelle, C., Sauvaud, J. A., et al. 2016, SSRv, 200, 495
Samson, J. A. R., & Gardner, J. L. 1973, JChPh, 58, 3771
Schlag, E. W., Frey, R., Gotchev, B., Peatman, W. B., & Pollak, H. 1977, CPL, 51, 406
Shematovich, V. I., Bisikalo, D. V., Gérard, J. C., et al. 2008, JGRE, 113, E02011
Shirai, T., Tabata, T., & Tawara, H. 2001, ADNDT, 79, 143
Simon, C., Witasse, O., Leblanc, F., Gronoff, G., & Bertaux, J. L. 2009, P&SS, 57, 1008
Skrzypkowski, M. P., Gougousi, T., Johnsen, R., & Golde, M. F. 1998, JChPh, 108, 8400
Soret, L., Gérard, J.-C., Libert, L., et al. 2016, Icar, 264, 398

Soret, L., Gérard, J.-C., Schneider, N., et al. 2021, JGRA, 126, e29495
Steffl, A. J., Young, L. A., Strobel, D. F., et al. 2020, AJ, 159, 274
Stevens, M. H., Evans, J. S., Schneider, N. M., et al. 2015, GeoRL, 42, 9050
Stevens, M. H., Siskind, D. E., Evans, J. S., et al. 2019, JGRE, 124, 1226
Strickland, D., Bishop, J., Evans, J., et al. 1999, JQSRT, 62, 689
Strobl, K. H., & Vidal, C. R. 1987, JChPh, 86, 62
Tanaka, Y., Jursa, A. S., & LeBlanc, F. J. 1960, JChPh, 32, 1199
Tokue, I., Shimada, H., Masuda, A., Ito, Y., & Kume, H. 1990, JChPh, 93, 4812
Tsurubuchi, S., & Iwai, T. 1974, JPSJ, 37, 1077
Xu, S., Mitchell, D., Liemohn, M., et al. 2017, JGRA, 122, 1831
Yung, Y. L., & Demore, W. B. 1999, Photochemistry of Planetary Atmospheres (New York: Oxford Univ. Press)
Zubek, M., Olszewski, R., & Wolinski, P. 1997, JPhB, 30, L791